ISSN 1882-3432

TECHNOLOGY DEVELOPMENT CENTER NEWS
NATIONAL INSTITUTE OF INFORMATION AND COMMUNICATIONS TECHNOLOGY
Serial No. 38 December 2019

CONTENTS

Proceedings of the 17th NICT TDC Symposium (Kashima, June 27, 2019)

- News - News - News - News -

VLBI at 230 GHz using SPART toward EHT and EAVN -hi-

Takahiro Aoki[1] (*t-aoki@yamaguchi-u.ac.jp*), **Hiroyuki Maezawa**[2], **Sho Masui**[2], **Daiki Tsukiyama**[2], **Ayaka Tomihara**[2], **Nozomi Okada**[2], **Atsushi Nishimura**[2], **Hideo Ogawa**[2], **Kotaro Niinuma**[1], **Ryoko Amari**[1], **Toshihisa Tsutsumi**[1], **Kenta Fujisawa**[1], **Yoshinori Yonekura**[3], **Yasuhito Kamichi**[3], **Makoto Inoue**[4,5]

1. Yamaguchi University, Japan; 2. Osaka Prefecture University, Japan; 3. Ibaraki University, Japan; 4. Academia Sinica Institute of Astronomy and Astrophysics, Taiwan; 5. National Astronomical Observatory of Japan, Japan

Abstract: We conducted international VLBI observations at the 230 GHz frequency using the SPART 10-m antenna of the Osaka Prefecture University at the Nobeyama Radio Observatory in Japan. Stations that participated in the VLBI were the GLT 12-m in Greenland, the SRAO 6-m in Korea, and the SPART. This paper briefly summarizes the temporal VLBI system of the SPART and the observations. The data are under correlation at the Shanghai Astronomical Observatory and the results will be reported later. The observations are expected to lead to joining the EHT and developing the EAVN at high frequency.

1. Introduction

The Event Horizon Telescope (EHT) took an image of the shadow of the black hole in the center of M87, which was published on April 10, 2019. Seeing implementation of such global millimeter/submillimeter very long baseline interferometry (VLBI) observations, we successfully tested interferometry at the 230 GHz frequency or the 1.3 mm wavelength using the 10-m Solar Planetary Atmosphere Research Telescope (SPART) and the 1.85-m antenna of Osaka Prefecture University. Advancing the millimeter-wave interferometry, we conducted international VLBI observations using the SPART on March 18 and 19, 2019, one month before the press release of the M87 black hole image, and gained a foothold in joining the EHT. Stations in the VLBI observations are the SPART 10-m in Japan, the GLT 12-m in Greenland, and the SRAO 6-m in Korea. The 230 GHz VLBI observations are expected to lead to the EHT and also the EAVN -hi- (East-Asian VLBI Network at high frequency).

This paper elaborates on the project in Section 2, the system setup of the SPART in Section 3, and the observation in Section 4. Note that this paper focuses the SPART and does not describe the other stations. The observation data are under correlation and the result will be reported at another time.

2. The Project

This project is to test the millimeter-VLBI (mm-VLBI) at 230 GHz using three antennas of the the GLT 12-m in Greenland, the SRAO 6-m in Korea, and the SPART 10-m in Japan. The correlation of the observation data is supposed to be accomplished by the Shanghai Astronomical Observatory (SHAO) in China. A VLBI station in Japan will be important to enhance the EHT capability. Aiming to join the EHT and extend the frequency coverage of the EAVN, we planned the project and defined its purpose and immediate goal as follows.

2.1 Purpose

The purpose of this project is to reveal structural variation of active galactic nuclei (AGNs). If an AGN erupts a jet with high speed, the structure of the central region should vary in a short time. Observations with high cadence and angular resolution are required to detect such short timescale structural variation. That is why we planned VLBI observations twice a short period between March 17 and 21, 2019. The actual observations were executed on March 18 and 19 considering the weather and the status of all the stations. Targets are seven AGNs of 3C345, 1633+382, 1928+738, 3C371, M87, NGC6251, and 1653+3945.

2.2 Success Criteria

The immediate goal for the above science is to acquire VLBI fringes. Then we, the SPART team, define the success criteria are as follows:

Minimum Success To participate in the international mm-VLBI using the SPART and try to detect fringes.

Full Success To detect fringes of baselines including the SPART.

Extra Success To acquire VLBI images to which the SPART contributes.

As of the writing of this paper, we have already achieved the minimum success, that is to say, we have completed the observations and transported the data to the SHAO for correlation.

3. System Setup

The configuration of the SPART for the observations is described in Table 1. The start frequency

Table 1. Configuration of SPART

Position	$(-3871061, 3428327, 3723784)$ m
Slew speed	0.1 deg/s
Elevation	30–80 deg
Aperture eff.	0.4 at 230 GHz
Frequency	230.200–230.712 GHz
Polarization	single linear
Sampling	1024×10^6 sample/s
Quantization	2 bit/sample

was 230.200 GHz among all the stations; however, there are differences in bandwidth and polarization between the stations. The bandwidths of the GLT, SRAO, and SPART are 2048 MHz, 1024 MHz, and 512 MHz, respectively, and also the polarizations are dual circular, single circular, and single linear. The recording system used at the GLT and SRAO was the R2DBE/Mark6 and that at the SPART was the ADS3000+/OCTAVE. The position of the SPART was estimated using the Google map and a handy GPS receiver, which may cause a positional error of tens of meters.

3.1 System Layout

Figure 4 shows the SPART and two sheds used for the observations and Figure 5 shows the system block diagram. VLBI equipments were installed in the Shed 1 and a GPS antenna was tied on a laundry pole on its wall. We laid two coaxial cables between the SPART and the Shed 1 for transporting the inter-mediate frequency (IF; 0–1 GHz) and 10 MHz reference signals. The 100 V power is distributed from the Shed 1 to the Shed 2 and the maximum current capacity is 30 A; therefore, we had to switch off some unnecessary instruments.

3.2 Receiver

The receiver block diagram and frequency conversion are indicated in Figure 6. Considering the specification of signal-generators used as local oscillators (LOs), we set frequencies of the first LO, f_1, and the second LO, f_2, to

$$f_1 = 224\ 187\ 999\ 978 \text{ Hz},$$
$$f_2 = 5\ 500\ 000\ 022 \text{ Hz}.$$

This setting enabled us to acquire an IF signal of 512–1024 MHz corresponding to 230.200–230.712 GHz. The band-characteristics of the receiver is shown in Figure 1. Note that no frequency-filters existed before the first LO and hence the acquired IF signal had a double sideband as shown in Figure 6. We confirmed that the frequency setting was correct through an observation of the CO($J = 2-1$) line of DR21 as shown in Figure 2.

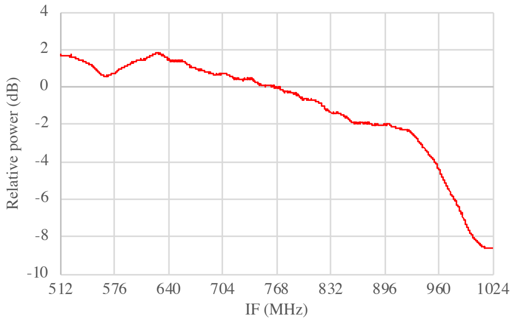

Figure 1. Band-characteristics of the system.

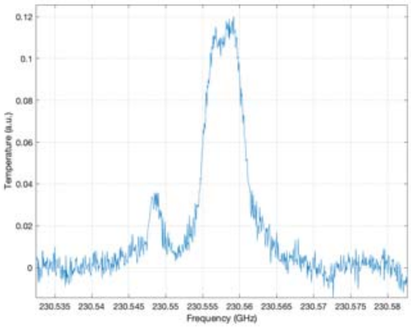

Figure 2. CO($J = 2-1$) line of DR21 observed on March 17.

3.3 Analogue-to-Digital Conversion

We input the 512–1024 MHz IF signal to the analogue-to-digital converter (ADC) ADS3000+ with parameters listed in Table 1. Note that the high-order sampling of the 512–1024 MHz analogue signal by the 1024 MHz sampling rate inverted the band of the digital data. The data handling requires attention to the bit sequence because the OCTAVE system, the interface between the VLBI Standard Interface and the 10 Gbps Ethernet, reverses the least significant bit and the most significant bit.

3.4 Clock

The 10 MHz reference signal is supplied to the SPART as shown in Figure 5. Then, we transported the signal from the SPART to the VLBI instruments in the Shed 1 via the 30 m coaxial cable. The phase stability of the reference system was not measured but expected enough for the VLBI observations.

The one pulse per second (1PPS) signal is not supplied to the SPART. Therefore, we should have created the signal using the GPS receiver. The time lag between the 1PPS signals of the ADC and the GPS was displayed on a time-interval counter

Table 2. VLBI Schedule

Start UTC	Duration [s]	Target
11:00:00	1200	M87
11:23:00	1200	M87
11:46:00	1200	M87
12:09:00	1200	M87
12:32:00	1200	M87
12:59:00	1200	NGC 6251
13:22:00	1200	NGC 6251
13:49:00	1080	3C 371
14:10:00	1080	3C 371
14:35:00	1080	1928+738
14:56:00	1080	1928+738
15:17:00	1080	1928+738
15:42:00	1200	3C 345
16:05:00	1200	3C 345
16:29:00	1200	1633+382
16:52:00	1200	1633+382
17:16:00	1200	J1653+3945
17:39:00	1280	J1653+3945

but not monitored/recorded by a computer. We can not know the drift of the 1PPS offset but think the offset was maintained within 1.3 μs by our visual management.

4. Observation

The observations were performed on March 18 and 19, 2019. The VLBI schedule is indicated in Table 2. Although the weather was not fine, there were no problems with the source tracking, 1PPS offset, and lock status of the LOs. There was a concern about a power level; we noticed that an offset level of power measured by a power meter occasionally and suddenly increased or decreased due to unidentified cause. However, the power jump did not occur during the observations and thus the observations were thought to be succeeded.

Figure 3 shows system noise temperatures including atmospheric contribution, T^*_{sys}, defined as

$$T^*_{\mathrm{sys}} = \frac{T_{\mathrm{R}}}{P_{\mathrm{Sky}}/P_{\mathrm{R}} - 1},$$

where T_{R} indicates a temperature of a black body of a chopper wheel, P_{Sky} a power received when observing the sky, and P_{R} a power received when observing the black body. The system noise increased when the weather was cloudy but decreased to about 200 K on the latter half of the observation on March 19 under a clear sky.

5. Summary

We conducted international VLBI observations at 230 GHz or 1.3 mm using the GLT 12-m, SRAO 6-m, and SPART 10-m antennas with the aims of joining the EHT and developing the EAVN at high frequency. For the observations, we temporally installed the VLBI equipments in the SPART as detailed in Section 3. The observation data are under correlation at the SHAO and the results will be reported later.

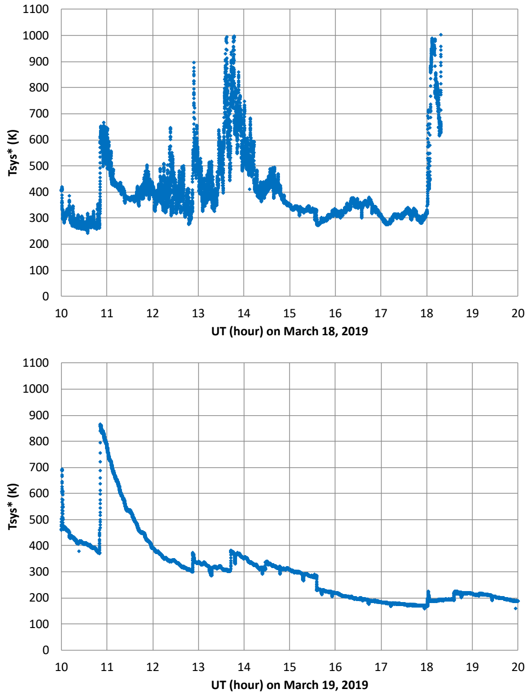

Figure 3. Time series variation of the system noise temperatures.

6. Acknowledgments

We are grateful to the members of the Nobeyama Radio Observatory, especially Dr. Minamidani, for considering our implementation plan and providing advice for us.

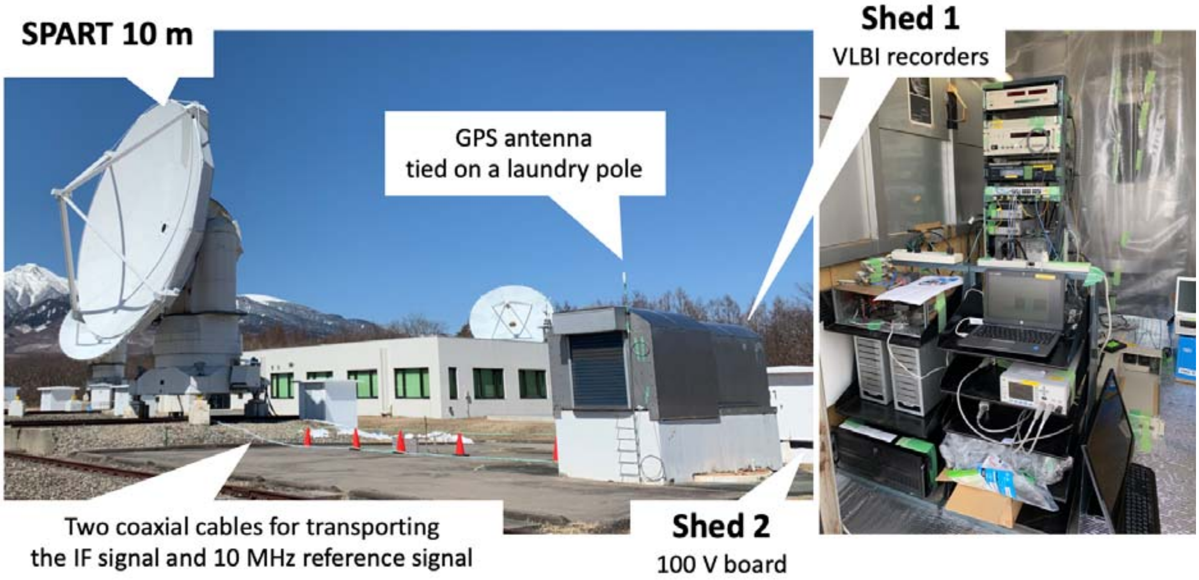

Figure 4. System layout.

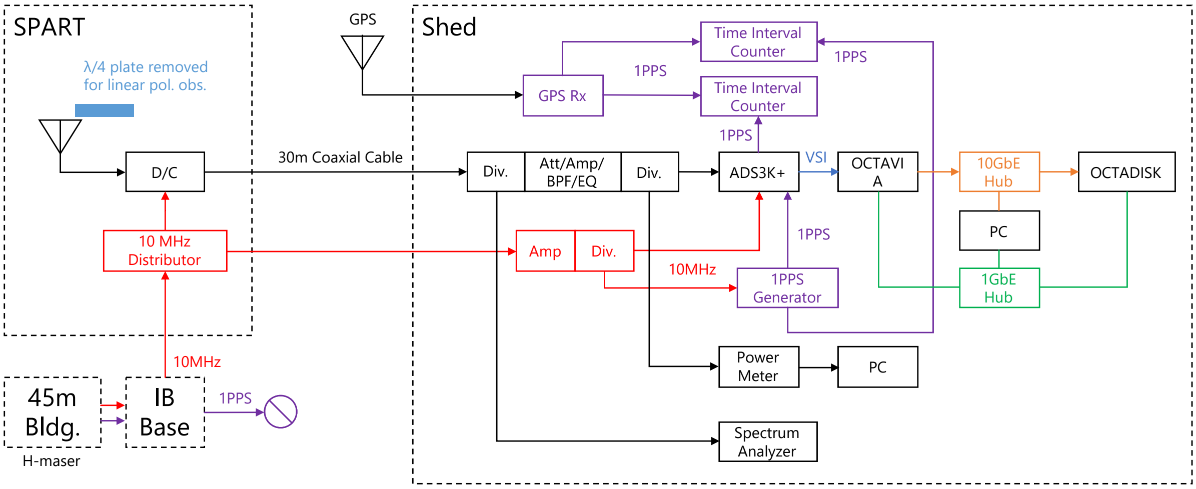

Figure 5. System block. The 'Shed' indicates the Shed 1 in Figure 4.

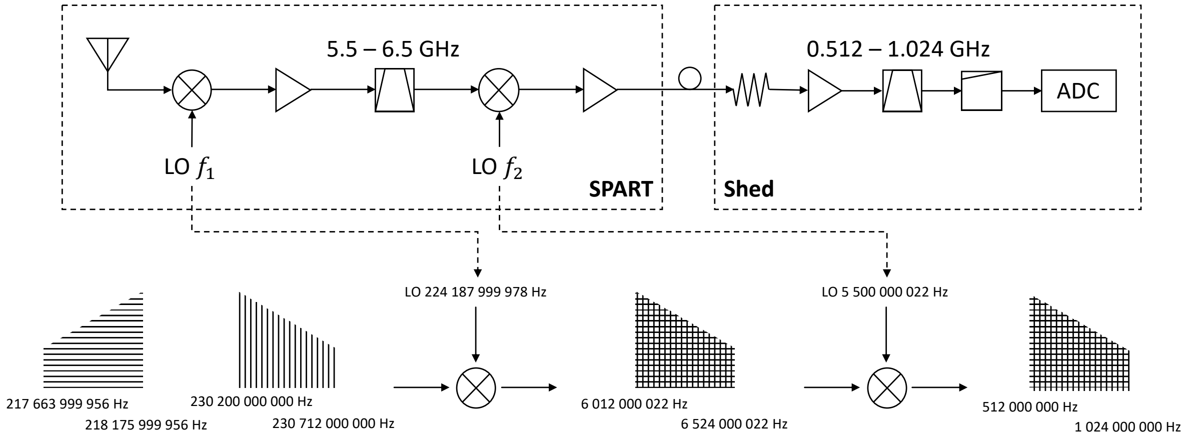

Figure 6. Receiver block diagram and frequency conversion.

Water vapor detection under rainy weather condition

Noriyuki Kawaguchi (*kawagu.nori@nao.ac.jp*),

National Astronomical Observatory of Japan,
2-21-1 Osawa, Mitaka Tokyo, Japan

Abstract: Water vapor radiometers are used to compensate for atmospheric absorption and delay that have a significant effect on radio astronomy and VLBI observations. The atmospheric absorption is important to know the absolute brightness of an observing target, and the atmospheric delay is important to correct a delay time to be measured by VLBI for true geometrical delays to get better vertical solutions. Correction of the delay time is indispensable not only for precise geodetic measurement by VLBI and GPS but also for accurate astrometric positioning of celestial targets by VLBI. The water vapor radiometer, however does not work well under a bad weather condition. This article shows a new water vapor radiometer which introduces advanced digital technology to detect a wide band spectrum of atmospheric emission. The new water vapor radiometer makes it possible to separate the emission spectrum of water vapor from the absorption spectrum of liquid water, making it possible to measure only water vapor in the atmosphere, even under dense clouds or during rainfall.

1. Introduction

A water vapor radiometer, WVR, is an essential device that corrects unwanted effects such as absorption and delay caused by liquid water and water vapor in the atmosphere during radio astronomy and VLBI observations. The absorption is important to know absolute brightness of celestial targets in accurate radio photometry. The delay is important to reduce geometrical delays which are key observables in precise geodetic measurements by VLBI and GPS, and astrometric measurements by VLBI as was noted in Kawaguchi(2017)) [1].

A new water vapor radiometer reported in this paper, which has been developed by the National Astronomical Observatory of Japan, NAOJ, since 2017. The new radiometer was successfully demonstrated and confirmed for its high performance, ability to detect minute amount of water vapor even in bad weather conditions.

Section 2 states that currently widely used water vapor radiometers have large measurement errors under bad weather conditions such as dense cloud and heavy raining. Examples of comparison results from the VLBI campaign of EURO-76 and measurement results at the Shanghai Observatory are shown. The large error is caused by insufficient separation of brightness temperatures of water vapor and liquid water.

Section 3 shows the difference between the emission spectra of water vapor and liquid water. The difference in the spectra is very effective for separating water vapor and water droplets.

Section 4 presents the results of water vapor radiometer measurements operated under dense clouds and heavy raining, and shows the successful detection of a very small amount of water vapor in the sky.

Section 5 concludes that ultra-wide band digital spectral measurements are important to separate water vapor from liquid water.

2. A large error of WVR under cloudy and rainy weather

The bad behavior of WVR responses in a geodetic VLBI campaing, EURO-72, was reported by Jungho Cho(2006)[2]. He operated the Wettzel WVR simultaneously with geodetic VLBI observations. The records of VLBI delay and the WVR delay are shown in Figure 1. Under a clear sky the WVR delay shows good agreement with VLBI delay but under a rainy sky the WVR delay is much larger than the VLBI delay.The large difference may have caused by the liquid water, which raises the sky brightness temperature much higher than the expected radiation of water vapor by absorption. It should be noted that the liquid water raise the noise temperature by absorption, but without delay. We need to carefully remove the liquid absorption temperature from the total sky brightness temperature to derive the true water vapor delay.

The SHAO WVR is a WVR operated by Shanghai Astronomical Observatory for working with the Tianma 65-m radio telescope. As was noted in Kawaguchi(2016)) [3], the WVR does not work well under the bad weather condition. In Figure 2 the Excess Path Length, EPL, measured independently by three different ways, GPS delays expressed by red dots, ray tracing delays by open squares and SHAO WVR by blue dots.

When the weather is good until around 9 o'clock, the results of the three measurements agree well, but when the clouds begin to appear at around 10 o'clock, the delay measurements by WVR gradually get larger and larger apart from the other two

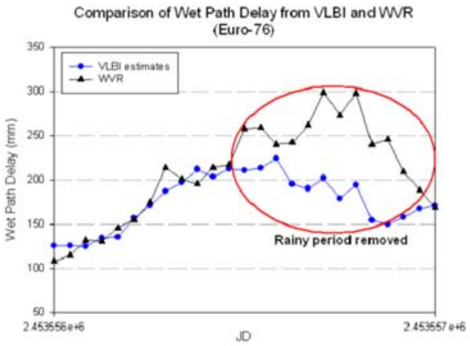

Figure 1. Delay comparfison Wettzel WVR EPL and VLBI delay

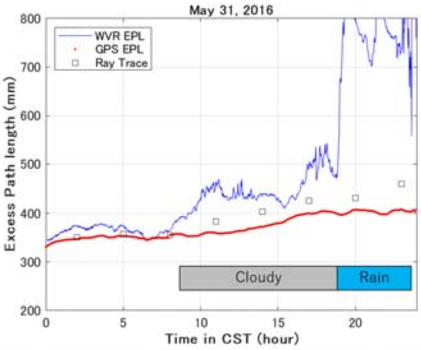

Figure 2. SHAO WVR under cloudy and rainy weather

results. The difference becomes extremely large when it started raining at night. The delay measurements by WVR were no longer incredible. Although liquid water raises the sky noise temperature very high but does not cause any delay,

Similar extraordinary measurements by WVR was reported in Ichikawa(2006)[4] in CONT05 VLBI campaign. Zenith wet delays measured by WVR, GPS, VLBI and radiosondes were compared each other. As shown in Figure 3, the WVR delay also shows extraordinary large values at under bad weather.

3. Liquid and Vapor Emission

As noted in the previous section, separation of water vapor and liquid water is a key to derive the true EPL of water vapor alone exactly. Only way to separate the liquid water from the water vapor is to measure the broad band spectrum. The liquid absorption spectrum is almost linear with respect to frequency. On the other hand, the emission spectrum of water vapor shows a characteristic resonance spectrum centered at a frequency around 22.2 GHz as shown in Figure 4.

In the figure, water vapor emission spectrum is indicated by a blue curve and liquid absorption spectrum is plotted with a red line. True brightness temperature of a water vapor is a height above the red straight line of a liquid water spectrum.

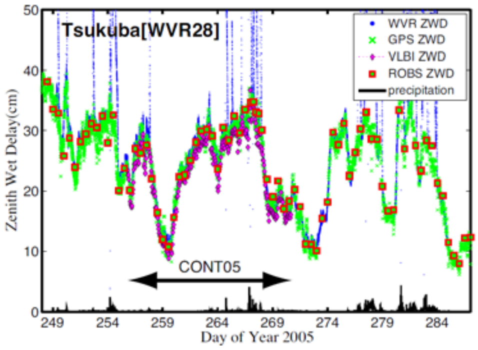

Figure 3. Zenith wet delay comparison during CONT05 VLBI campaign

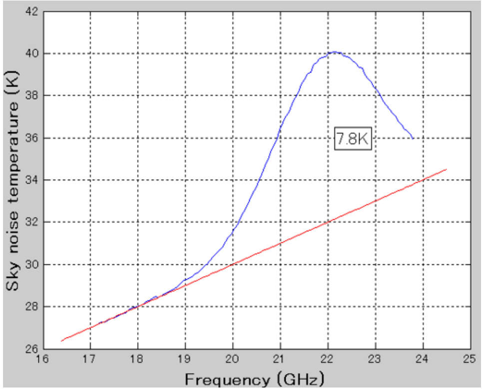

Figure 4. Spectra of water vapor and liquid water emissions

The liquid water in a cloud and a rain significantly raise sky noise temperature. To get true brightness of water vapor emission, contribution of the liquid water needs to be subtracted. The cloud absorption and the noise temperature is shown in Figure 5 for a frequency range from 16GHz to 24GHz in case of a cloud named 'Cumulus-cumulus Congestus', one of nine cloud types classified by Slobin(1982)[5]. The cloud contains liquid water $0.57g/m^3$ in the density distributed over the height from 660m and 3400m above sea level. This type of a cloud causes the largest attenuation and biggest raise of sky noise temperature.

In Figure 6, liquid water emission temperatures at three frequencies around 22GHz, a resonance frequency of water vapor are calculated in the rain rate up to 40mm/hour in the maximum according to a theoretical estimation made by Shambayati(2008)[6].

In Figure 7, liquid water spectrum under raining

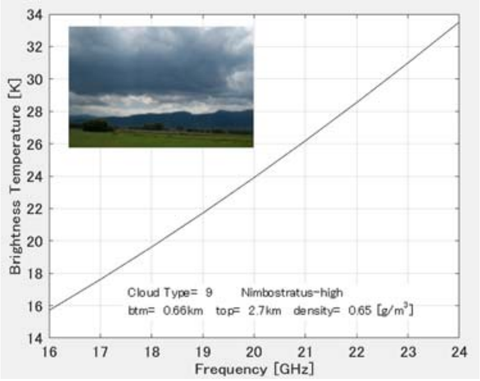

Figure 5. Liquid absorption temperature under thick cloud

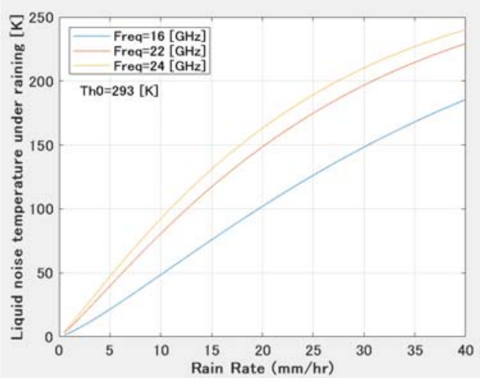

Figure 6. Liquid water emission temperature under raining

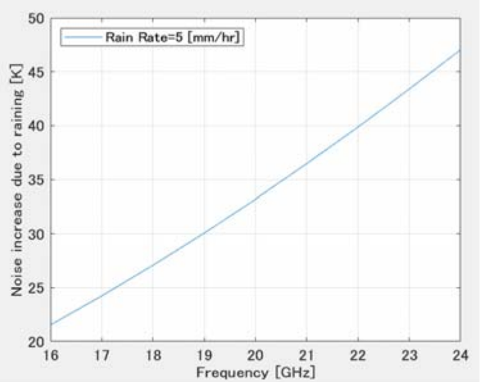

Figure 7. Increase of a sky noise temperature caused by liquid water at a rain rate of 5mm/h

at the rain rate of 5mm/hour is shown. The rainfall is not so unusual, and radio astronomy observations are often performed even under such rainfall. The noise temperature reaches up to 40K. Also we can see in Figure 7 that the liquid noise temperature is almost linearly increasing with frequencies at a frequency range from 16GHz to 24GHz.

4. A new WVR operated under bad weather condition

In June, 2018 a new WVR was set right next to the radio astronomy receiver on the VERA 20-m radio telescope as shown in Figure 8. Since the installation position is offset from the radio astronomy receiver, the WVR beam is not exactly directed to the celestial target but ignored in this experiment. The water vapor radiometer measures the amount of water vapor very close to the radio astronomical beam toward the target. Since the horn for the water vapor radiometer is slightly smaller, it irradiates an area larger than the size of the sub-reflector, causing a large spillover loss and lowering the aperture efficiency, but the beam size formed by the main reflector is almost the same as the radio astronomical beam. The lower efficiency is not fatal to monitor the water vapor emission, the strength of which is strong enough, an order of a few tens kelvin.

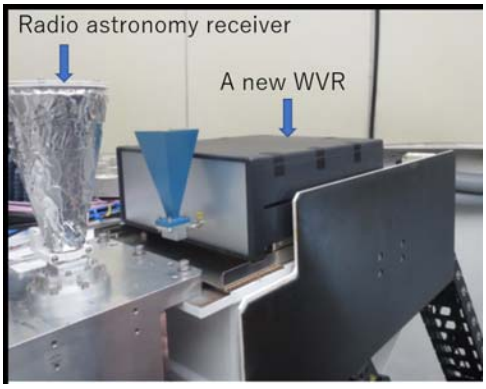

Figure 8. A new WVR on the VERA 20m radio telescope

While the WVR was tested on the VERA telescope, the weather was very bad. A thick cloud covers over the telescope as shown in Figure 9, and it started raining and at occasionally strong raining of 6mm/hour was recorded by a rain meter shown in Figure 10.

Figure 9. Weather condition, cloudy and raining

In Figure 11 the sky noise spectrum is shown,

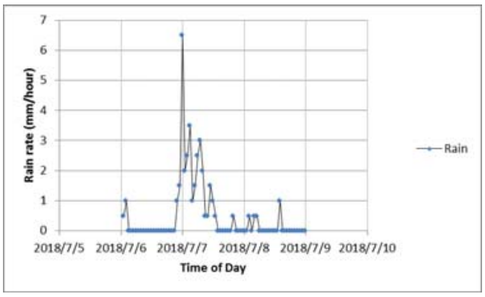

Figure 10. Rainmeter record

which was observed during heavy rain. This spectrum is almost a straight line, and the spectrum peculiar to water vapor seen around 22 GHz is hardly seen. However, detailed analysis confirmed the presence of a small 3K water vapor.

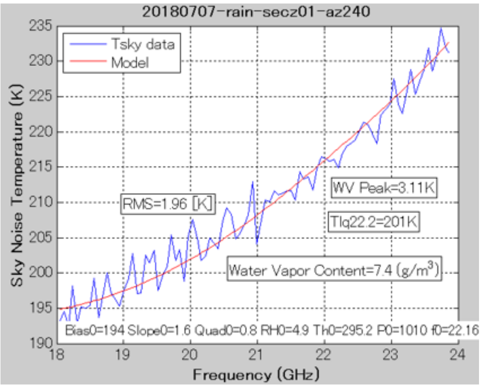

Figure 11. Tipping results under raining

The correctness of this small amount of water vapor was confirmed by lowering the elevation angle. In Figure 12, the horizontal axis indicates the radio wave path length (secZ, $Z = 1/sin(El)$) traveling through atmosphere, and the vertical axis indicates the noise temperature radiated by water vapor and liquid water.

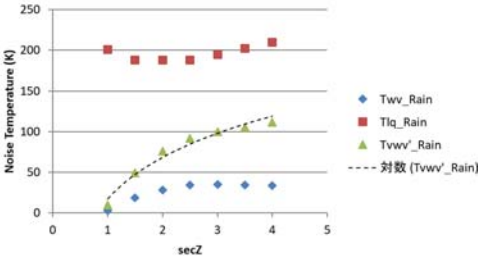

Figure 12. Water vapor spectrum under heavy raining

The measured noise temperature of water vapor is indicated by blue diamonds. The radiation intensity of very little water vapor increases as the elevation angle decreases (as the path length of the atmosphere increases), but is saturated in very low elevations. The noise temperature of liquid water is indicated by red squares. The attenuation is evaluated by $\alpha = \frac{T_{liq}}{T_{atm}}$, where T_{liq} is a noise temperature of liquid water and T_{atm} is atmosphere temperature. If T_{liq} equals to the atmosphere temperature (around 300K), the correction coefficient, $\frac{1}{1-\alpha}$, becomes infinity, the sky is completely opaque. The liquid noise temperature of around 200K in Figure 12 indicates that the heavy attenuation of 67% exists. The water vapor radiation is saturated in low elevations, which is thought to be due to the attenuation by liquid water. The emission intensity of water vapor corrected for the absorption is indicated by green triangles. Although the absorption was corrected, the emission intensity of water vapor was found not to be proportional to $secZ$ but to follow $log(secZ)$. The logarithmic dependence was confirmed in various azimuth angles and different weather conditions. It is very strange that the water vapor emission has been believed to be proportional to the path length of the atmosphere, $secZ$. This should be studied more in future.

5. Cocluding Remarks

In this paper I presented the water vapor detection under bad weather conditions, the success of a weak water vapor emission about 3K in the noise temperature. So far almost all WVRs in the world shows extraordinary increase of wet delays in bad weather conditions. It was concluded that this was caused by incomplete separation of the emission spectrum of water vapor and the absorption spectrum of liquid water.
The logarithmic dependence of the water vapor radiation intensity on the atmospheric path length has not been elucidated yet and needs to be investigated further in the future.

References

[1] Noriyuki Kawaguchi, Water Vapor Radiometer for Radio Astronomy and Volcano Monitoring, Technology Development Center News, National Institute of Information and Communications Technology, Serial No. 37, page 5, June 21, 2017

[2] Jung-ho Cho, Axel Nothnagel, Alan Roy, and Ruediger Haas, A generalized scheme to retrieve wet path delays f rom water vapor radiometer measurements applied to European geodetic VLBI network, 4th IVS General Meeting, Concepcion, Chile, Jan. 9-11, 2006

[3] Noriyuki Kawaguchi, Water Vapor Radiometer: Challenge Again, Technology Develop-

ment Center News, National Institute of Information and Communications Technology, Serial No. 36, page 4, November 2016

[4] Ryuichi Ichikawa, Hiromitsyu Kuboki, Masanori Tsusumi, Yasuhiro Koyama, Junichi Fujisaku, Kensuke Kokado, Masayoshi Ishimoto and Kazuhiro Takashima, Zenith wet delay comparisons at Tsukuba and Kashima VLBI stations during the CONT05 VLBI campaign, Japan Geoscience Union Meeting, August 2006

[5] Stephen D. Slobin, Microwave noise temperature and attenuation of clouds: Statistics of these effect at various sites in the United States, Alaska, and Hawaii, Radio Science, Volume 17, Number 6, pages 144 3- 1454, November-December 1982

[6] Shervin Shambayati, Atmosphere Attenuation and Noise Temperature at Microwave Frequencies, DESCANSO Book Series, volume 10, chapter 6, p. 255, February 2008

Current Status of TEC Estimation in the Wideband Bandwidth Synthesis Software

Testuro Kondo[1,2] (*kondo@nict.go.jp*,
kondo@shao.ac.cn)
and Kazuhiro Takefuji[1,3]

[1]*Kashima Space Technology Center,*
National Institute of Information
and Communications Technology,
893-1 Hirai, Kashima, Ibaraki 314-8501, Japan
[2]*Shanghai Astronomical Observatory,*
80 Nandan Road, Shanghai, 200030, China
[3]*ISAS/JAXA after Oct.1, 2019*

1. Introduction

An algorithm using the least-squares estimation based on a phase model was developed for determining TEC in the wide-band bandwidth synthesis (WBWS) processing [*Kondo and Takefuji*, 2016]. The algorithm works well. However, it is difficult to apply this algorithm for data of which SNR lower than 10. In order to improve a TEC estimation at lower SNRs, we have developed a TEC search-function method in addition to the least-squares estimation method.

2. TECs obtained by the least-squares (LSQ) estimation using a phase model

Table 1 shows a VLBI experiment used for this report and Fig. 1 shows the location of baseline.

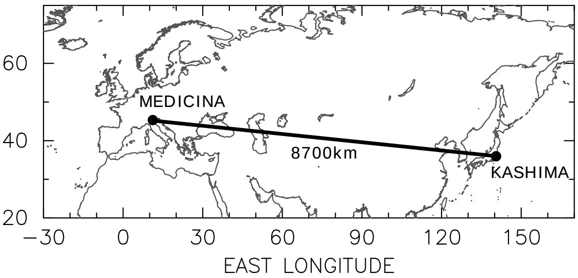

Figure 1. Location of baseline.

In the LSQ method, phase characteristics of cross-spectrum with respect to frequency after the wide-band bandwidth synthesis (WBWS) processing are modeled as follows.

$$\theta(f) = 2\pi f\{\Delta\tau + \Delta\tau_{ion}(f)\} + \phi_0 \qquad (1)$$

where f, $\Delta\tau$ and ϕ_0 are an RF frequency, a residual delay and a constant phase, respectively, and $\Delta\tau_{ion}(f)$ is a delay caused by the ionosphere which is given as

Table 1. VLBI experiment used here

Baseline	Kashima - Medicina (about 8700 km)
Date (UT)	2018/10/05(278) 07:01 – 10/06(279) 14:57
Polarization	H (Horizon)
Receiving Frequency (GHz)	
Band#1	5.490 – 6.514
Band#2	7.990 – 9.014
Band#3	9.890 – 10.914
Band#4	12.790 – 13.814
# of scans	592

$$\Delta\tau_{ion}(f) = \alpha f^{-2}\Delta TEC \qquad (2)$$

where ΔTEC is the difference of TECs in the propagation paths leading to each station, and α is a constant ($= 1.34 \times 10^{-7}$ m^2/s). Hence Eq.(1) can be written as follows.

$$\theta(f) = 2\pi(f\Delta\tau + \alpha f^{-1}\Delta TEC) + \phi_0 \qquad (3)$$

$\Delta\tau$, ΔTEC and ϕ_0 are estimated by using a least-squares method [*Kondo and Takefuji*, 2016].

Fig. 2 shows a comparison of TECs obtained by the LSQ method using a phase model and those obtained from a TEC global map provided by IGS [*IGS CDDIS DAAC*, 2018]. One sigma error after a linear fitting is 3.24 TECU (TECU $= 1.0 \times 10^{16}$ electron/m^2). Fig. 3 shows a histogram of the number of scans succeeded in TEC estimation and that of failed scans for SNRs. As shown in Fig. 3, almost all scans of which SNR lower than 10 are failed in TEC estimation. The success ratio is only 66 %.

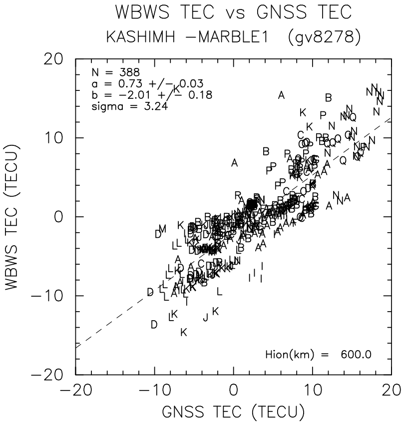

Figure 2. A comparison of TECs (WBWS TEC) obtained by the LSQ method and those (GNSS TEC) obtained from a TEC global map.

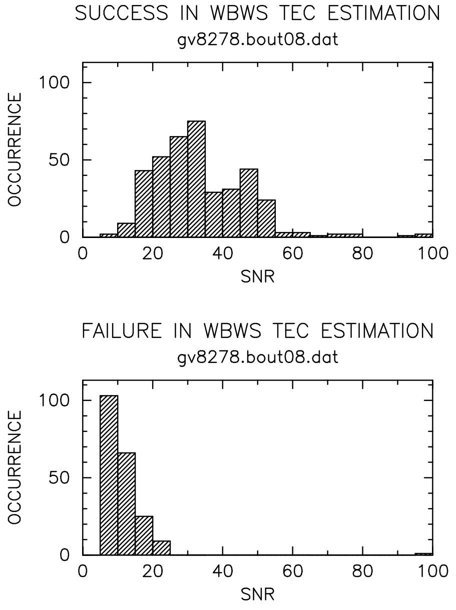

Figure 3. A histogram of the number of scans succeeded in TEC estimation (upper panel) and that of failed scans (lower panel) for SNRs.

In order to improve the success ratio at lower SNRs, we have developed a new method based on a search function similar to that for delay and delay rate search (maybe it is a similar idea adopted in the HOPS post-processing software [*Cappallo*,2014]).

3. A TEC search function

A search function like that used for delay and delay rate search is introduced here for a TEC estimation as follows.

$$F(\Delta\tau,\Delta\dot{\tau},\Delta TEC) = \left|\int_{t_0}^{t_1}\int_{f_0}^{f_1} S_{wc}(f,t)e^{-i\theta(f,t)}df\,dt\right| \qquad (4)$$

where $\Delta\dot{\tau}$ is a residual delay rate, $S_{wc}(f,t)$ is a wideband cross-spectrum at time t after the correction of inter-band delay differences and inner-band phase characteristics, and $\theta(f,t)$ is a phase term at t that is given as

$$\theta(f,t) = 2\pi f\{\Delta\tau + \Delta\dot{\tau}t + \Delta\tau_{ion}(f)\} + \phi_0 \qquad (5)$$

where ϕ_0 is a constant phase, and $\Delta\tau_{ion}(f)$ is a delay caused by the ionosphere and given by Eq.(2).

Assuming that $\Delta\dot{\tau}$ is determined well with a sufficient accuracy by a WBWS process, we can integrate over time at first. Moreover $|e^{-i\phi_0}| = 1$, hence, a search function can be re-written as follows.

$$\begin{aligned} &F(\Delta\tau,\Delta TEC) \\ &= \left|\int_{f_0}^{f_1} S_{wc}(f)e^{-i2\pi f(\Delta\tau+\alpha f^{-2}\Delta TEC)}df\right| \\ &= \left|\int_{f_0}^{f_1} S'_{\Delta TEC}(f)e^{-i2\pi f\Delta\tau}df\right| \qquad (6)\end{aligned}$$

where

$$S_{wc}(f) = \int_{t_0}^{t_1} S_{wc}(f,t)e^{-i2\pi f\Delta\dot{\tau}t}dt$$

and

$$S'_{\Delta TEC}(f) = S_{wc}(f)e^{-i2\pi\alpha f^{-1}\Delta TEC} \qquad (7)$$

The integral portion of Eq. (6) is an expression in the form of a Fourier transform regarding $\Delta\tau$, so that we can use FFT for calculation of this portion by calculating $S'_{\Delta TEC}(f)$ at first.

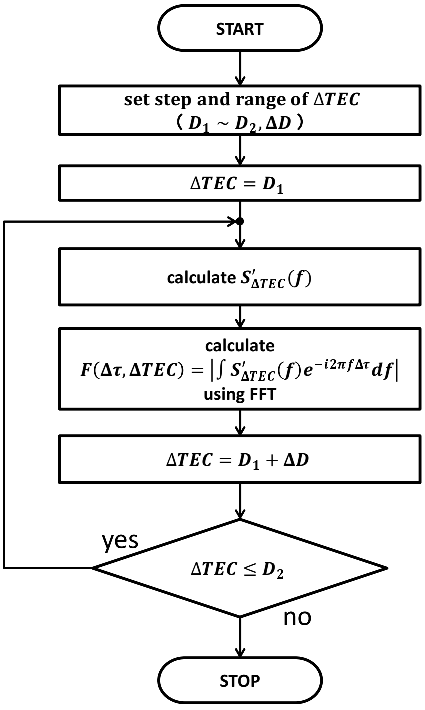

Figure 4. A flow of calculation of TEC search function.

The specific search procedure is shown in Fig. 4. First, decide the range of ΔTEC as $D_1 \sim D_2$ and step ΔD. Set $\Delta TEC = D_1$, then calculate $S'_{\Delta TEC}(f)$. Using this $S'_{\Delta TEC}(f)$, calculate Eq. (6) by using FFT. Increase ΔTEC by ΔD, then do the same calculation. Repeat this process until $\Delta TEC = D_2$.

Values of $F(\Delta\tau,\Delta TEC)$ calculated this way are those on grid points shown in Fig. 5. An example of an actual search function is shown in Fig. 6. Estimation of TEC is given as ΔTEC that shows the largest value of search function. The position of actual maximum value is usually determined by a parabolic approximation, because a true peak position is shifted from the grid point.

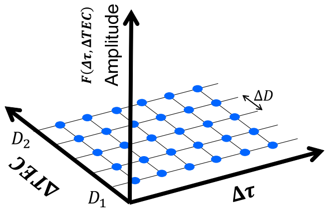

Figure 5. Values of search function are obtained for grid points regarding ΔTEC and $\Delta\tau$.

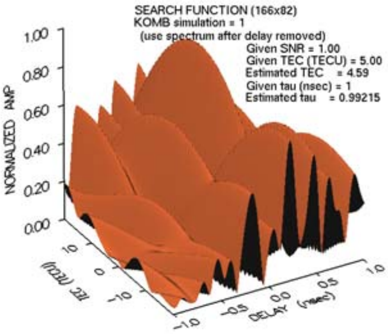

Figure 6. An example of TEC search function. ΔTEC covers from -20 TECU to $+20$ TECU. The value of a search function is calculated by using FFT at each grid point using a given ΔTEC.

Fig. 7 shows a comparison of TECs obtained by the TEC search function method and those obtained from a TEC global map. One sigma error after a linear fitting is 2.95 TECU. It's slightly improved compared to that of the LSQ method. Fig. 8 shows histogram as same as Fig. 3. As shown in the figure, we can see the remarkable improvement of the success ratio at lower SNRs. Total success ratio has increased to 98 %.

4. Conclusions

We have been improving a TEC estimation in the WBWS software. The success ratio of TEC estimation by introducing a TEC search function. It has prominently improved the success ratio of TEC estimation at lower SNRs.

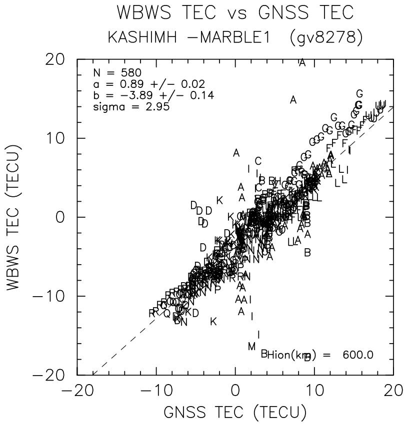

Figure 7. A comparison of TECs (WBWS TEC) obtained by a TEC search function method and those (GNSS TEC) obtained from a TEC global map.

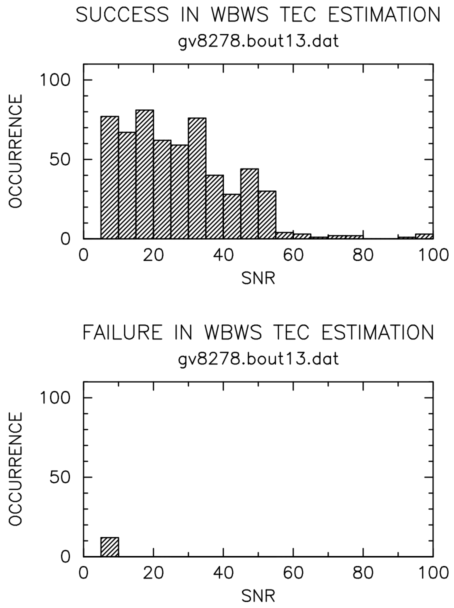

Figure 8. A histogram of the number of scans succeeded in TEC estimation (upper panel) and that of failed scans (lower panel) for SNRs. The success ratio at lower SNRs is remarkably improved.

One sigma error when compared with GNSS is about 3 TECU. We were expecting a smaller one sigma error considering from the results of the short baseline experiments that were carried out in Japan. The difference in spatial resolution of the ionosphere is considered as one of the causes. The spatial resolution of a global TEC map obtained by GNSS observations is only a few hundred kilometers. On the other hand, TEC estimated from

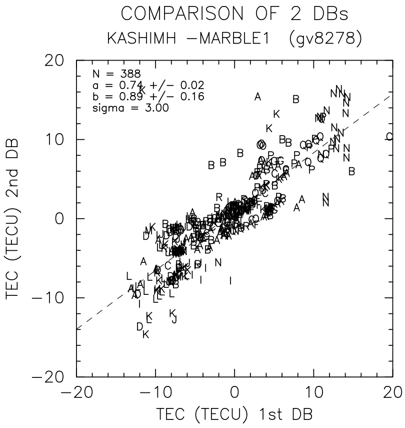

Figure 9. A comparison of TECs obtained by the GM method (horizontal axis) and the PM method (vertical axis).

VLBI data thought to be reflected a smaller spatial scale.

Another possibility is that this represents an actual estimation error. Fig. 9 shows a comparison of TECs obtained by the GM method and the PM method. It's one sigma error after linear fitting is about 3 TECU. If the error of both is about the same, each error is $3/\sqrt{2} = 2.1$ TECU. In addition, a clear band-split structure can be seen in the scatter plot, which is also seen in Fig. 2. Whether it reflects the actual condition of the ionosphere or not is being considered.

Acknowledgement: A wide band VLBI experiment used in this report was carried out under the cooperation between NICT, INAF (Italian National Institute for Astrophysics) and INRIM (Italian National Metrology Institute). We would like to thank staff members of INAF and INRIM engaged in the experiment. A part of this work has been funded by Chinese Academy of Sciences (CAS) President's International Fellowship Initiative, Grant No. 2018VEA00017.

References

Cappallo, R., Correlating and fringe-fitting broadband VGOS data, *IVS 2014 General Meeting Proceedings*, pp.91–96, 2014.

Crustal Dynamics Data Information System (CDDIS DAAC), 2018. International GNSS Service, Ionosphere vertical total electron data. Available online [http://cddis.gsfc.nasa.gov/Data_and_Derived_Products/GNSS/atmospheric_products.html#iono] from NASA EOSDIS CDDIS DAAC, Greenbelt, MD, USA., Subset obtained: time period: 2018-278 to 2018-279.

Kondo, T., and K. Takefuji, An algorithm of wideband bandwidth synthesis for geodetic VLBI, *Radio Sci.*, Vol. 51, doi:10.1002/2016RS006070, 2016.

VLBI-GNSS Collocation Survey at the Ishioka Geodetic Observing Station

Saho Matsumoto
(*matsumoto-s96n2@mlit.go.jp*),
Michiko Umei, Haruka Ueshiba,
Shinobu Kurihara, Takahiro Wakasugi,
Tadao Kikkawa and Hirosi Munekane

Geospatial Information Authority of Japan, 1 Kitasato, Tsukuba Ibaraki, Japan

Abstract: The International Terrestrial Reference Frame (ITRF) is realized by a combination of solutions of four different space geodetic observing techniques. To perform this combination, it is necessary that relative position between these space geodetic observing instruments, namely local-tie vectors, are precisely known at collocation sites where observing instruments of multiple space geodetic techniques are installed. The Ishioka Geodetic Observing Station (hereafter referred to as the Ishioka station), is one of such collocation sites that has a VLBI and two GNSS stations. To measure the local tie vector between them, which is defined as the vector between the invariant point (IVP) of the VLBI antenna and the GNSS reference point, we conducted the collocation survey in November 2018 there. In this survey, we adopted two methods to determine the IVP: "Outside method" and "Inside method". We compared the results of them, and confirmed that "Inside method" produces the local-tie vector which is of the similar quality as that of "Outside method" which is well established. Since "Inside method" is more practical than "Outside method", we decided to adopt it for future collocation surveys.

1. Introduction

The International Terrestrial Reference Frame (ITRF) is realized by a combination of solutions of four space geodetic observing techniques (VLBI, SLR, GNSS and DORIS), where VLBI solutions contribute in determining the scale and EOP. In order to achieve combination of different solutions, it is necessary to prepare relative positions between the instruments at a collocation site which has two or more space geodetic observing instruments. The Ishioka station operates a VLBI and two GNSS stations. The VLBI station is one of the VLBI Global Observing System (VGOS) stations which is promoted by International VLBI Service for Geodesy and Astrometry (IVS) as the next-generation standards (Ishimoto et al., 2016), and one GNSS station, "ISHI", is registered as one of the International GNSS Service (IGS) sites. To measure the local-tie vector between the VLBI and the GNSS station, which is defined as the vector between the VLBI antenna invariant point (hereafter referred to as the IVP) and the reference point of the IGS station ISHI, we conducted the collocation survey in November 2018 at the Ishioka station.

2. Purpose of this study

Figure 1 shows a panoramic view of the Ishioka station. Four pillars and a VLBI ground marker are installed there. "ISK2" is an experimental CORS (Continuously Operating Reference Station). The collocation survey was performed using these pillars and the VLBI ground marker for determining the local tie vector. The IVP of the VLBI antenna is defined as the intersection of the azimuth (hereafter referred to as AZ) and elevation (hereafter referred to as EL) axes. It must be determined indirectly since it is not directly observable. There are two methods to estimate the IVP. One is "Outside method" where we observe targets attached on the moving parts (near the counterweight) of the VLBI antenna with "Total Station" (hereafter referred to as TS) on the reference pillars shown in Figure 1. The other is "Inside method" where we observe the targets on a cabin wall from a cabin pillar that is detached from the antenna moving parts. We had only experiences of the "Outside method" so far, but the Ishioka VLBI antenna allows us to carry out the "Inside method" thanks to its cabin pillar structure. In the "Inside method", it is expected that the observation error would be less than the "Outside method" because TS is set up closer to the targets. In addition, with the "Inside method", it might be easier to estimate the offsets and axes orthogonality between the AZ and EL axes than the "Outside method", since TS observations may be done evenly for every AZ/EL direction. We conducted the collocation survey using both methods in November 2018 to examine whether the "Inside method" may be adopted instead of "Outside method".

3. Observations

The collocation survey was performed from 8th to 22nd in November 2018. We conducted it by following three processes.

3.1 Surveys between pillars and VLBI ground marker

We measured the horizontal and vertical angles, and distances between the pillars and the VLBI ground marker with a TS. Then we performed lev-

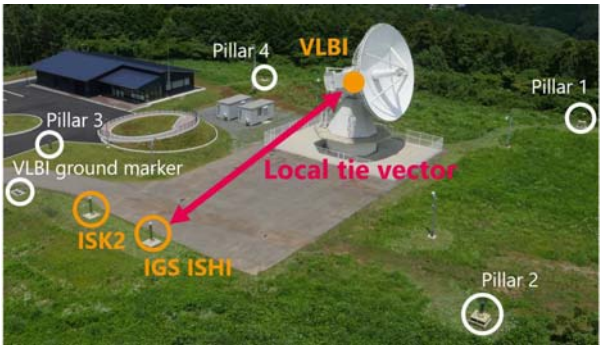

Figure 1. Panoramic view of the Ishioka station. Four pillars and a VLBI ground marker are arranged around the VLBI antenna and GNSS stations.

eling surveys among them to determine relative heights. In addition, we conducted GNSS surveys at the pillar 2 and 3, and a reference point at the top of Mt. Tsukuba in order to determine the orientation angle of the local frame so that we can convert the survey results in a geocentric reference frame.

3.2 Surveys between pillars and IGS station

We measured the horizontal angles and distances between the pillars and the IGS station. Since the antenna reference point (hereafter referred to as ARP) of the IGS station is not directly observable due to the redome, it must be determined indirectly. Therefore we measured the horizontal angles at the left and the right end of the choke ring antenna, and used their mean value. Regarding the distance from the pillars to the IGS station, we first measured the shortest distance from each pillar to the bottom of the choke ring antenna, and then calculated the distance from the pillars to the ARP using the design value of the antenna. In addition, we measured the relative height from pillars to the GNSS reference point and from the GNSS reference point to the bottom of the antenna by the leveling surveys, respectively. The sum of these may be considered as the height of the ARP. Figure 2 shows the survey diagram about above two processes (3.1, 3.2).

3.3 Determination of the IVP of VLBI antenna

3.3.1 Outside method

We installed the target outside the moving parts of the VLBI antenna (upper left in Figure 3). Then we observed the target from the TS installed on the pillars while changing the AZ and EL angles of the antenna (right in Figure 3). We pointed the VLBI antenna to 8 direction around the AZ axis and 5 direction around the EL axis for each AZ direction. Observed targets should be on the imaginary spherical surface (lower left in Figure 3), and we can consider the center of it would be the IVP.

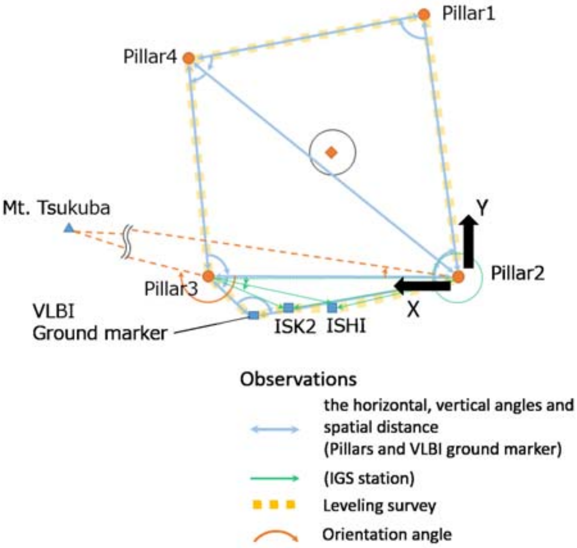

Figure 2. Observation diagram of the collocation survey in 2018 (except the determination of the IVP).

3.3.2 Inside method

We observed the targets from the TS installed inside cabin pillar of the VLBI antenna (right in Figure 4). First we observed the targets on surrounding pillars to determine the position of the TS. Then we installed the targets on the cabin wall of the AZ cabin and carried out measurements for determining the AZ axis. We set the antenna EL to zero, and observed four targets while changing the antenna AZ by 30 degree from 0 to 330 degree (left in Figure 5). Then we carried out measurements for determining the EL axes. In order to investigate the dependency of the estimated EL axes on different azimuthal direction, we tentatively estimated the EL axes at the AZ of 125 degree and 215 degree. For each antenna AZ, we observed two targets while changing the antenna EL by 10 degree from 0 to 90 degree (right in Figure 5). In total, we obtained 48 target positions for the determination of the AZ axis and 40 target positions for the determination of the EL axes. We fit circles to trajectories of the target and the AZ axis is estimated as a straight line connecting the center of these circles. The EL axis is estimated in the similar way as that of the AZ axis. Then the IVP

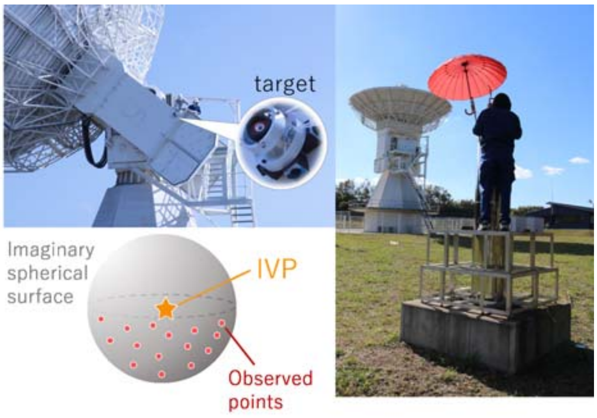

Figure 3. Observation of the "Outside method" for estimating the IVP. The TS was put on the pillar and moved to other pillar according to the AZ rotation.

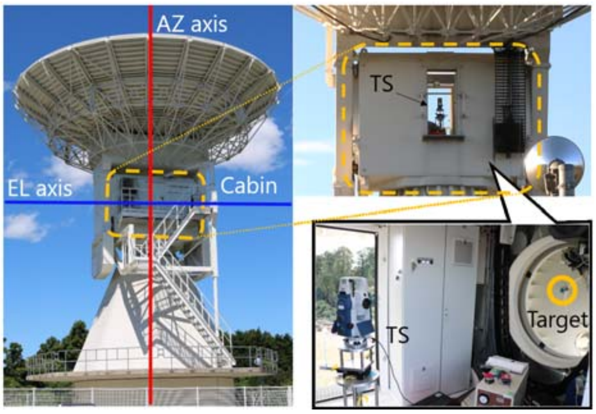

Figure 4. Observations inside the antenna cabin for estimating the azimuth and elevation axes. The TS was put on the cabin base, which does not follow the antenna movement.

is defined as the closest point between the AZ and the EL axes.

4. Result

Table 1 shows the IVP coordinates determined by both methods and their differences. Note that these coordinates are expressed in the "local frame" whose origin lies on Pillar 2 and X axis is aligned with the line from the Pillar2 to Pillar3 (Figure 2). The differences are negligibly small. Then we determined the offsets and orthogonality between the axes with the "Inside method" (Figure 6). Offsets between the AZ axis and the EL axes for AZ of 125 degree and 215 degree were 0.2 mm and 0.1 mm, respectively. The angles between the AZ axis and two EL axes were 90.0006 degree and 89.9955 degree, respectively. Finally, we calculated the local-tie vector between the IVP of VLBI antenna and the IGS reference point with the "Inside method" in the geocentric frame (Table 2). To confirm our calculation by the "Inside method", we independently calculated the local-tie vector with the adjustment software pyaxis (LINZ, 2015). We found that the differences of the local tie vectors between those by our calculations and those by pyaxis were negligibly small in practical use. The standard deviations of the local-tie vector for the "Inside method" estimated using pyaxis are as small as 0.7 mm, 0.7 mm, and 0.6 mm for x, y, and z component, respectively. In terms of the number of staff and working hour, the "Inside method" is more efficient than the "Outside method" (Table 3) because we observe the target only from the cabin base for the "Inside method" instead from four pillars as done for the "Outside method". From the results, we confirmed that the "Inside method" has sufficient accuracy and it is more practical. In this sense, the "Inside method" can be adopted as an alternative to the "Outside method".

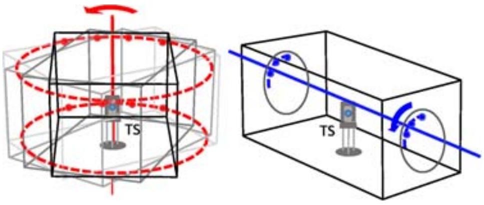

Figure 5. Observations of the targets on the cabin wall. We observed the targets from the TS while rotating the antenna AZ(left) and EL(right).

Table 1. IVP coordinate (※ According to the "local frame" whose origin lies on Pillar 2 and X axis is aligned with the line from the Pillar2 to Pillar3 (Figure 2))

	X	Y	Z
Outside method (m)	31.4824	30.7626	9.2577
Inside method (m)	31.4841	30.7623	9.2570
Δ(mm)	-1.7	0.3	0.7

5. Summary

We conducted the collocation survey at the Ishioka station in November 2018. We determined IVP position using two methods independently, the "Inside method" and the "Outside method". We compared the results of two methods and confirmed that the "Inside method" could be a practical alternative to the "Outside method" in terms of its accuracy and efficiency. With the "Inside method", it may be possible to conduct a collocation survey more frequently since it takes less time to survey. We will submit the estimated local-tie vector to the

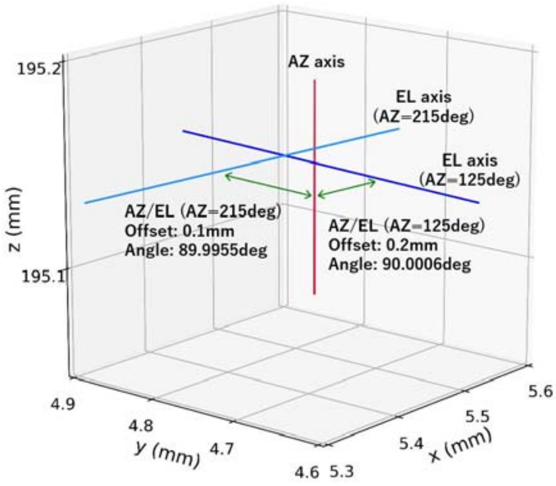

Figure 6. Offsets and the orthogonality of the axis.

Table 2. The estimated local tie vector between the IVP of the VLBI antenna and ISHI in the geocentric reference frame

	X	Y	Z	Baseline
Inside(m)	-12.7427	10.8579	-37.0948	40.6976
Inside(m) (pyaxis)	-12.7410	10.8611	-37.0962	40.6992
Δ(mm)	-1.7	-3.2	1.4	-1.6

Table 3. The comparison of personnel and working hour of between two methods.

	day	the number of staff
Outside method	7	6 ∼ 9
Inside method	1	5

International Earth Rotation and Reference Systems Service (IERS) to be used in the construction of the next ITRF.

6. Acknowledgments

We would like to thank the Land Information New Zealand (LINZ) for making the pyaxis software publicly available (https://github.com/linz/python-linz-pyaxis).
We acknowledge Dr. Chris Crook at LINZ for his assistance for the use of the software.

References

[1] Ishimoto M., M. Umei, T. Wakasugi, R. Kawabata, T. Toyoda, B. Miyahara, T. Fukuzaki, Status on the Ishioka Geodetic Observing Station, IVS NICT-TDC News, vol.36, pp.9-12, 2016.

[2] Land Information New Zealand, 2015 - Warkworth Observatory Local Tie Survey.

The VLBI survey of Extremely Compact HII regions associated with a high mass star just after nuclear ignition using Kashima - Hitachi baseline

Tatsuya Ogura, Kazuhito Motogi, Takahiro Aoki, Kotaro Niinuma, Kenta Fujisawa (Yamaguchi Univ.) Yoshinori Yonekura (Ibaraki Univ.) Mamoru Sekido, Kazuhiro Takefuji (National Institute of Information and Communications Technology)

Abstract: A size of infant HII region created by a high mass star just after the nuclear ignition is decided by a gravitational radius for ionized gas. This size is expected to be about 100 astronomical unit (au). Physical parameters (mass, luminosity, etc) of host stars exciting such an Extremely Compact (EC) HII region give strong observational constraints on a theoretical evolutionary model of a high mass protostar. But, the angular size of such a newborn HII region is very small ($\sim$ 100 mas), because high mass star-forming regions are mostly located on beyond 1 kpc from the Earth. Therefore, a high-sensitivity single-baseline VLBI is a useful tool to survey such EC HII regions, because one can selectively detect HII regions excluding other extended radio sources. For the above reasons, we started a new fringe survey towards known VLA radio sources using Kashima34m-Hitachi32m short-baseline VLBI having the angular resolution of 89 mas at X-band. The targets are 662 point-sources which detected by the 5GHz survey on Galactic plane using VLA (The CORNISH survey, $1''.5, 0.4$ mJy at 1σ). We selected infrared quiet sources out of the CORNISH sources. The most of selected targets are very radio quiet. The brightness-temperature sensitivity of the Kashima-Hitachi baseline is $\sim 10^3$K (600 sec at 1σ). This is enough sensitive to detect thermal free-free emission ($\sim 10^4$ K). We have already observed 270 targets on August 2019 and successfully detected fringes of 122 targets. They are plausible candidates of the EC HII region and we will conduct detailed follow-up studies by using J-VLA and ALMA.

1. Introduction

We are conducting a fringe survey using Japanese VLBI Network (JVN) sub-array which consists of Kashima, Hitachi, Takahagi, Yamaguchi-1st, and Yamaguchi-2nd stations (Figure 1). Our survey targets on a compact radio sources both inside and outside Galactic plane. There are three research topics : star-formation, active galactic nucleus, Galactic black hole. This paper focuses on a topic of the star-forming.

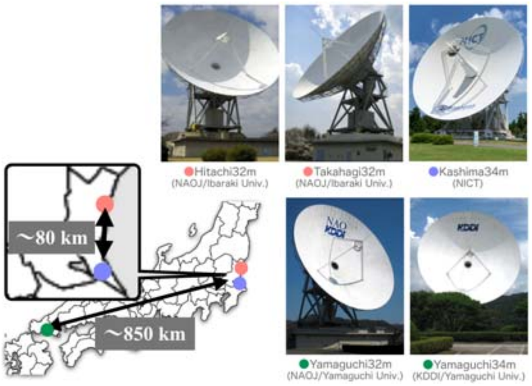

Figure 1. Array configuration and photos of each JVN station.

2. Infant HII regions associated with a newly-born high mass star

Ultraviolet radiation produced by a high mass star generates a region of ionized gas called the HII region. This section presents the size of infant HII regions associated with a high mass star just after nuclear ignition and its observational requirements.

2.1 A size of very young HII regions

A size of HII region formed by a high mass star just after the nuclear ignition depends on a relative size between the gravitational radius (r_g) and Strömgren radius (r_S). Equating the gravitational energy and the kinetic energy of ionized gas, r_g is shown as follows,

$$r_g \sim \frac{GM}{v_e^2} \tag{8}$$

where v_e is sound speed of the ionized gas (When $T_{\text{ionized gas}} = 10^4$ [K], $v_e = 13$ [km/s].). r_g is a radius in which the ionized gas can be confined by the stellar gravity. If r_g is larger than r_S, the radius of a HII region is given by r_g (Figre 2). Assuming $M = 20 M_\odot$ and $v_e = 13$ [km/s], r_g is $\sim$ 100 au.

Such an EC HII region is a plausible signature of such a very young star and has not been detected yet. If one can be detected the EC HII region, it is possible to give a strong limit on a theory of high mass stellar evolution based on several physical parameters (stellar mass, luminosity, etc...).

2.2 Obsercational requirements

Required array specifications for detectiong the EC HII region are as follows. The first request

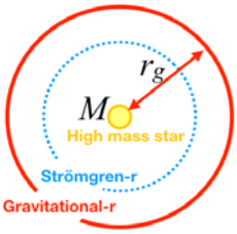

Figure 2. A size of HII region.

is high angular resolution : $\theta \sim 100$ [mas]. High mass star-forming regions are mostly located on $1-10$ kpc from Earth. Therefore, the angular size of its HII region ($r_g = 100$ [au]) is under 100 mas. The second request is high brightness-sensitivity : $T_b \sim 10^4$ [K]. One must detect thermal free-free emision ($\sim 10^4$ K). Brightness-sensitivity of $\sim 10^3$ K$/1\sigma$ is required.

3. Overview of the new fringe survey

This project is the first stage of EC HII region survey. To discover them, We are searching for compact radio objects ($\sim$ 100 mas) on Galactic plane using Kashima-Hitachi VLBI.

3.1 Targets

Targets were selected from the CORNISH survey (Hoare et al. 2012 [1]). This survey is a blind survey coordinated with the northern Spitzer GLIMPSE I region ($10° < l < 65°$, $|b| < 1°$) using VLA (5 GHz, $\theta = 1".5$, $\Delta S = 0.4$ mJy$/1\sigma$). The selected targets satisfy the following two characteristics : Infrared-quiet[1] and Point source against 1".5 beam. The distribution of targets is shown in Figure 3. Figure 4 shows that the most of selected sources have a low flux density of $0-10$ mJy at 5 GHz.

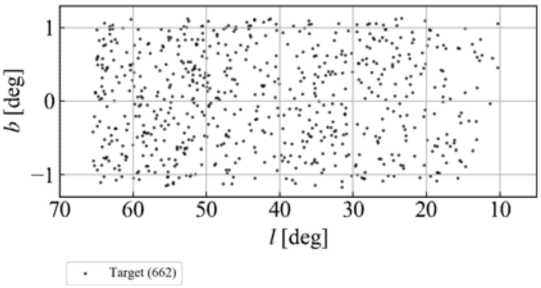

Figure 3. The distribution of targets.

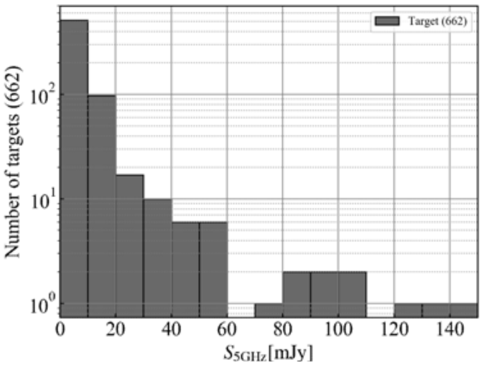

Figure 4. Flux of targets .

3.2 Observational method

This survey is performed in the single-scan snapshot-mode in which the integration-time is 10 min/source. The performance of Kashima-Hitachi array is shown in Table 1. Flux densities are calibrated by flux-calibrator NRAO530, adopting a single-dish flux taken by Hitachi telescope.

Table 1. The array performance

	Kashima-Hitachi VLBI
Band	8192 – 8704 MHz
Baseline-length	82.3337 km
Angular resolution	$\sim$ 89 mas (at max baseline-length)
Coherence-time	over 600 sec
Correlation	Software-correlator GICO3 created by NICT
Sensibility	From obsercational results, When $\Delta t = 600$ [sec], $1\sigma = 0.3 - 0.5$ [mJy] However, these value depend on projected baseline-lengths.

4. Progress

We have already observed 255 targets (Table 2). This chapter reports the progress to date (September 2019).

Table 2. Observational schedule

Date	Observational code	Number of targets
2019/2/21	U19052A	7
2019/7/10	U19191A	31
2019/7/11	U19192A	31
2019/7/25	U19206A	31
2019/7/26	U19207A	31
2019/7/27	U19208A	31
2019/8/7	U19219A	31
2019/8/8	U19220A	31
2019/8/9	U19221A	31

4.1 Detection statistics

Targets were recognized as a detection, when we could obtain a valid delay solution. Our detection criterion is that the resultant SNR ≥ 6 and residual-delay is ≤ 1 nsec. We detected 122 sources

---

[1] There are no mid-infrared Spitzer GLIMPSE I, $\lambda = 3.6, 4.5, 8.0$ μm point source within radius of 2". It is an index of young stars.

out of 255 targets (48 %). However, these detections contain several known species such as background AGN, and protostellar jets, young stellar object flares, etc. The spatial distribution in Galactic plane and histogram of Galactic longitude is shown in Figure 5 and Figure 6, respectively.

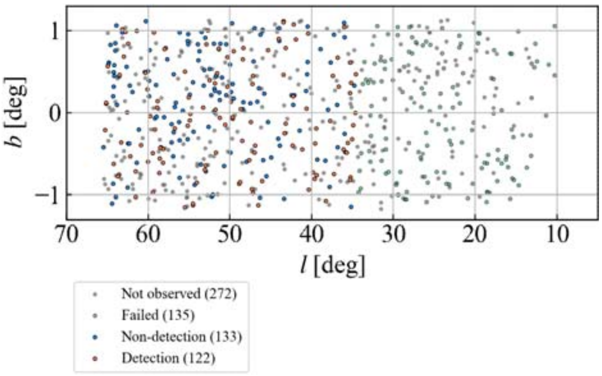

Figure 5. The distribution of detections.

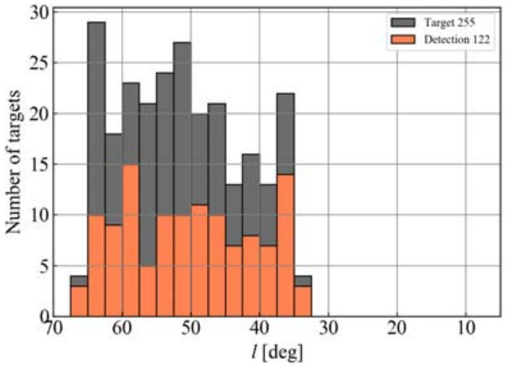

Figure 6. The histogram of detections.

4.2 Physical properties

Brightness-temperature $T_{B\min}$ and Spectral index ($\alpha_{\min}$) were estimated by observed flux as a lower limit.

Brightness-temperature: Figure 7 shows the histogram of $T_{B\min}$. There are many low-brightness sources of $10^4 - 10^5$ K. A temperature of an HII region could reaches a few 10^4 K in case of extremely optically thick condition. This might be a candidate of thermal free-free source (under investigation now).

Spectral index: Figure 8 shows the relation of $\alpha_{\min}$ and $T_{B\min}$. Most of the sources showed negative $\alpha_{\min}$, suggesting a non-thermal emission from AGN. On the other hand, positive $\alpha_{\min}$ is seen in some sources at 10^4 K $< T_{B\min} < 10^5$ K. Some of them may be an optically-thick thermal free-free source.

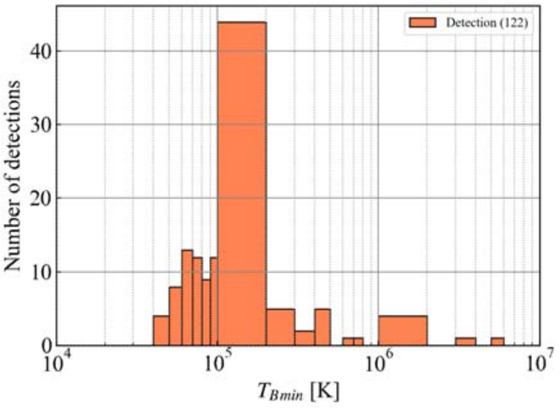

Figure 7. The histogram of $T_{B\min}$.

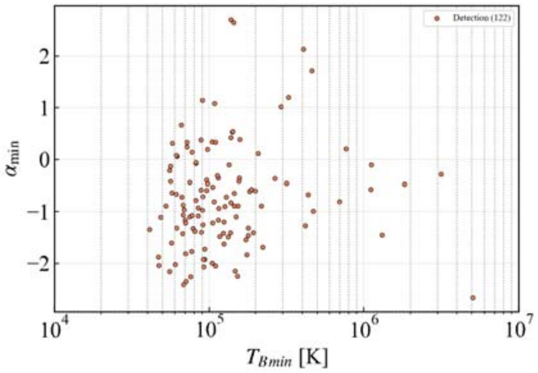

Figure 8. The spectral index between 5 GHz (The CORNISH survey) and 8 GHz (This work).

4.3 Next plan

Long-baseline Yamaguchi-Hitachi VLBI: As a next step, we identify compact non-thermal objects in detected samples by Yamaguchi-Hitachi VLBI. Any thermal sources should be resolved-out by 10 mas resolution. We already included Yamaguchi-Hitachi baseline in U19052A. We obtained 4 detections and 3 non-detections. The former showed high brightness temperatures of $T_{B\min} \sim 10^5$ K. They are clearly background AGN. The latter have a source size of $10 - 100$ mas, and can be a Galactic object. Other detected sources will be observed within this year.

Short-baseline Usuda-Hitachi VLBI: Unfortunately, Kashima telescope was destroyed by the typhoon No.15 in September 2019. However, we hope to complete this survey. Now, we consider to use another short baseline sub-array such as Usuda-Hitachi baseline. Figure 9 presents a projected baseline in different hour-angles. In some hour-angles, we can obtain similar baseline to that of Kashima-Hitachi VLBI.

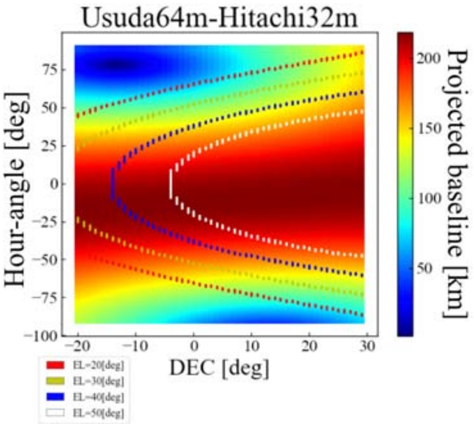

Figure 9. Projected baseline of Usuda-Hitachi VLBI.

5. Summary and Future work

The purpose of this survey is to discover candidates of the EC HII region. We have already observed 255 targets by using the Kashima-Hitachi VLBI. The detection rate in the short-baseline is 48 % and the detected samples could include candidates of thermal Galactic objects. The next plan is observing them using long-baseline VLBI to identify non-thermal objects. In addition, we will investigate details such as spectral index, spatial structure, etc for low brightness-temperature objects using VLA. On the other hand, we will also observe circumstellar structures using ALMA, studying the current stage of star-formation.

References

[1] M. G. Hoare, et al., 2012, PASP, 124, 939

Pulsar Observations in Japan: Leading Role of Kashima Observatory in 2009-2019

Toshio Terasawa (*terasawa@icrr.u-tokyo.ac.jp*),

ICRR, University Tokyo,
277-8582 Kashiwa-no-ha, Kashiwa, Chiba, Japan,
and, Mizusawa VLBI observatory, NAO,
181-8588 Osawa, Mitaka, Tokyo, Japan

Abstract: In 2009, we started Crab pulsar observation in collaboration with NICT colleagues in Kashima. Since then we have extended the observation network for pulsars, not only for the Crab pulsar but also for a magnetar XTEJ1810-197. In this paper I have reviewed our observational studies of pulsars in these 10 years.

1. Introduction

The Crab pulsar, one of the most famous pulsars, was discovered in 1968 [1], and has been playing the important roles in the basic study of pulsars (e.g., [2]). In these 10 years, we have made,

1. The first simultaneous multi-frequency detection of giant radio pulses from the Crab pulsar [3],
2. Search for the correlation between giant radio pulses and X-ray pulse intensities of the Crab pulsar [4],
3. Independent identification of the Crab pulsar's glitch in 2017 (Hisano et al., in preparation, 2019).

For the above study of the Crab pulsar we have organized the radio observation network in Japan combining Kashima observatory with other laboratories, the Usuda Deep Space Center (UDSC)/JAXA, the Iitate Planetary Radio Telescope (IPRT)/Tohoku University, the Center for Astronomy/Ibaraki University, the Research Institute for Time Studies (RITS)/Yamaguchi University, the Solar Wind Imaging Telescope (SWIFT)/Nagoya University, and the VLBI Exploration of Radio Astrometry (VERA) project/NAO.

In addition to these studies for the Crab pulsar, we have made,

4. Campaign observation of the radio outburst of a magnetar XTEJ1810-197 in 2018-2019 (Eie et al., in preparation, 2019).

In the following sections we summarize the results for the above four items.

2. Giant radio pulses from the Crab pulsar

A few pulsars, including the Crab pulsar, emit enigmatic sporadic intense radio pulses called 'Giant Radio Pulses' (GRP) (Fig. 1, 2) [5]. The flux distribution of GRP shows power-law dependence to the peak intensity (Fig. 3) in contrast to Gaussian or log-normal dependence to the peak intensity for ordinary pulses from the majority of other pulsars.

In [3], we made a simultaneous observation of GRP from the Crab pulsar with a frequency coverage from 0.3 GH to 8.4 GHz (widest-ever in 2016) in which the Kashima observatory provided 1.5-1.7 GHz data. Our observation showed that about 70% or more of the GRP frequency spectra are consistent with single power law with spectral indices from -4 to -1.

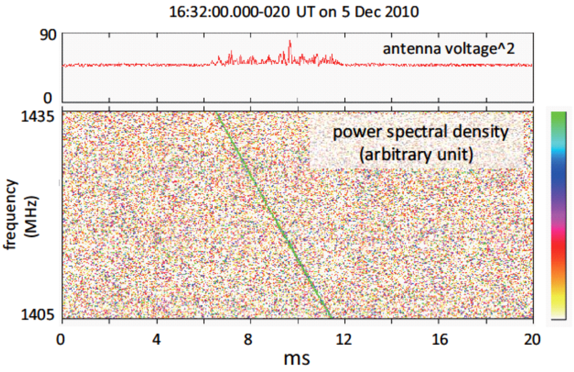

Figure 1. An example of a Crab pulsar's GRP observed in Kashima. The upper panel shows the variation of the squared antenna voltage (arbitrary unit) during a 20ms interval between 16:32:00.000 UTC and 16:32:00.020 UTC on 5 December 2010. The lower panel shows a corresponding dynamic spectrum, where the abscissa and ordinate show time and frequency. The power spectral density is shown in an arbitrary unit with pseudo-color. A GRP appeared as a green down-tone chirp signal from 1435MHz at ~6.5ms to 1405MHz at ~11.5ms.

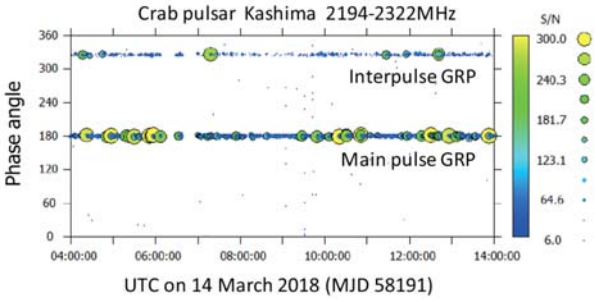

Figure 2. Giant radio pulses from the Crab pulsar observed in Kashima are shown in the rotation-phase-UTC diagram. Pulse intensities are shown in S/N with color-coded circles. Pulses clustering around 180° are of main-pulse GRP, and those around 326° are of interpulse GRP.

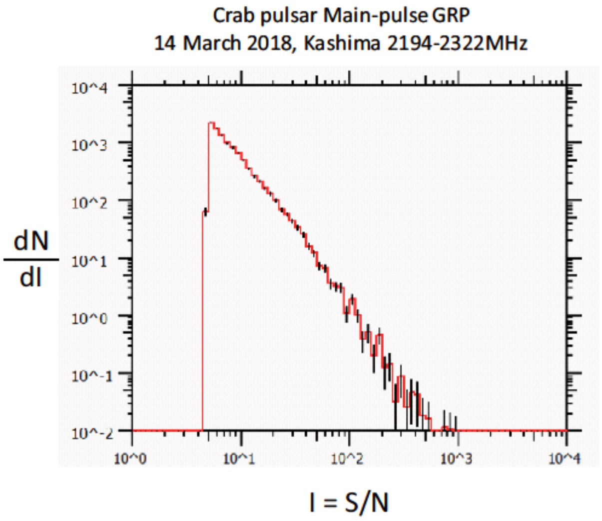

Figure 3. The flux distribution of the main-pulse GRP peak intensities in the 2.2-2.3GHz band.

3. Search for the correlation between giant radio pulses and X-ray pulses of the Crab pulsar

The Crab pulsar emits pulses in wide frequency range, coherently in radio band, and incoherently in optical to X/γ-ray bands. It is found that the optical pulses from the Crab pulsar show 3% enhancement (with 7.2σ significance) concurrent with GRP emissions in the radio band [6, 7]. While these detections imply that the incoherent optical emission is physically linked to the coherent radio emission, the mechanism of this linkage is not yet understood. Despite intensive efforts to search the correlation with radio emission at even higher energy bands, only upper limits have been obtained for X-ray and gamma-ray energy band [4, 8]. Contribution of the Kashima observatory was made in [4] where we did a correlational study of X-ray pluses from the Hitomi satellite and Crab's GRP from the Kashima observatory. We set ~22% upper limit of the X-ray enhancement (with 3σ significance) concurrent with the GRP emission in the radio band.

In 2017, the neutron star interior composition explorer (NICER), a payload of the international space station (ISS), started its X-ray observation (0.2-12keV) and improved the X-ray photon statistics by 1-2 or more orders of magnitude than the previous X-ray observations. In the period of 2017-2019, we conducted simultaneous X-ray pulse observation with NICER and GRP observations in Kashima and Usuda (UDSC) of the Crab pulsar (Table 1). The third column of Table 1, 'unassociated', shows the accumulated number of pulses other than GRP, while the fourth and fifth columns, 'MPGRP' and 'IPGRP', the accumulated numbers of main pulse and interpulse GRP, respectively. The sum of total numbers of pulses amounts to 4.21×10^6, which corresponds to the effective observation time of 39 hours.

Preliminary results show that there is a finite flux enhancement (several% with a significance more than ~4.5σ) of X-ray pulses concurrent with GRP. The detail of this correlation is now under investigation (Enoto et al., 2019, in preparation).

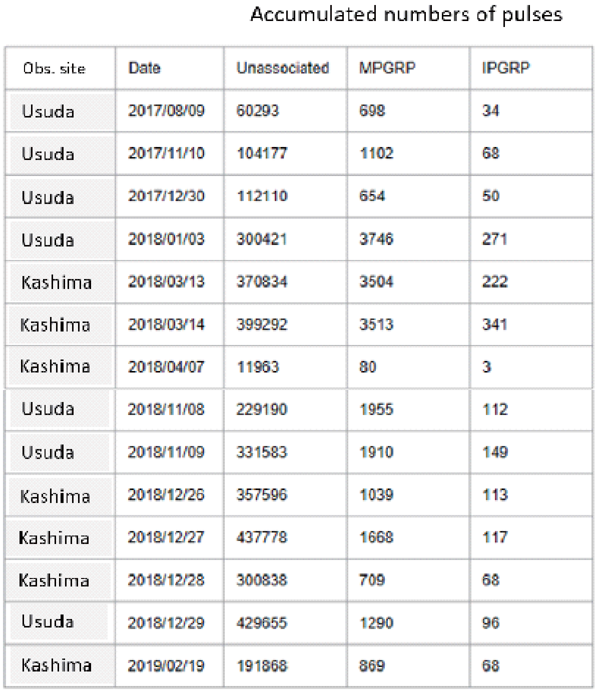
Accumulated numbers of pulses

Obs. site	Date	Unassociated	MPGRP	IPGRP
Usuda	2017/08/09	60293	698	34
Usuda	2017/11/10	104177	1102	68
Usuda	2017/12/30	112110	654	50
Usuda	2018/01/03	300421	3746	271
Kashima	2018/03/13	370834	3504	222
Kashima	2018/03/14	399292	3513	341
Kashima	2018/04/07	11963	80	3
Usuda	2018/11/08	229190	1955	112
Usuda	2018/11/09	331583	1910	149
Kashima	2018/12/26	357596	1039	113
Kashima	2018/12/27	437778	1668	117
Kashima	2018/12/28	300838	709	68
Usuda	2018/12/29	429655	1290	96
Kashima	2019/02/19	191868	869	68

Table 1. The accumulated numbers of pulses detected simultaneously both in radio and X-ray observations. Total numbers of pulses are 4,186,598, 24,537, and 1,712 for unassociated, MPGRP, and IPGRP, respectively.

4. The 2017 glitch of the Crab pulsar

The Crab pulsar has been monitored ~50 years since its discovery, and shown ~0.5Hz decrease from its value ~30.22Hz in 1969 [9]. This decrease occurred more or less continuously except sporadic spin-up events known as glitches, which are regarded as physical indicators of the coupling process between the outer region (the star crust + the magnetosphere) and the inner region (the superfluid star core) of the pulsar. On November 2017 there was an announcement of the largest-ever glitch detection for the Crab pulsar [10]. At this particular epoch, SWIFT/Nagoya University was conducting daily 325MHz band observation of the Crab pulsar, to prepare the solar corona observation at the time of the Crab pulsar's solar conjunction in June 2018 (Tokumaru et al., 2019, submitted to Solar Phys.). We then started our glitch search based on the SWIFT data, and confirmed the occurrence of this glitch (Fig. 4). While the daily Crab observation by SWIFT was the key of the identification of the glitch, the Kashima and IPRT data were indispensable in eliminating the $2\pi N$ uncertainty from the residual calculation. The details of the glitch parameters based on the SWIFT data are now being studied (Hisano et al., 2019, in preparation).

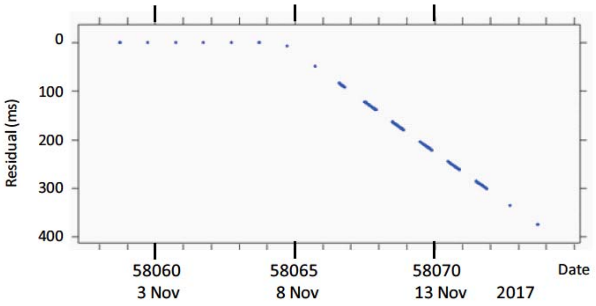

Figure 4. The residual of the arrival times of Crab pulses based on our radio observation: Till MJD 58063 (6 Nov. 2017), the pulse arrival times were consistent with the pre-glich model prediction [11], but showed the departure after MJD 58064. This is the evidence of the glitch on MJD 58064, and consistent with the individual result based on the Jodrell Bank observation [12].

5. The XTEJ1810-197 radio outburst in 2018-2019

Magnetars are one group of pulsar population with the characters of slow spin but fast spin-down, which are generally taken as the evidence of their very strong magnetic field (10^{14-15}G). While they were historically considered as radio-quiet, recent observations reveal radio outbursts from a few magnetars. Most recently, a magnetar called XTEJ1810-197 showed its second outburst early December 2018 [13].

We organized a ToO observation campaign for XTEJ1810-197 activating the Japanese network of pulsar observation with the frequency coverage from 325MHz to 22GHz, and identified pulses from this magnetar. During this campaign, Kashima observatory successfully provided the 2.2-2.3GHz band data (Fig. 5).

The flux distribution of pulses from XTEJ1810-197 (Fig. 6) shows a dependence to the peak intensity much softer than power law, in contrast to the Crab pulsar case (Fig. 3). Details of our observation are being studied (Eie, Master Thesis, Department of Astronomy, Univ. Tokyo, 2019; Eie et al., 2019, in preparation).

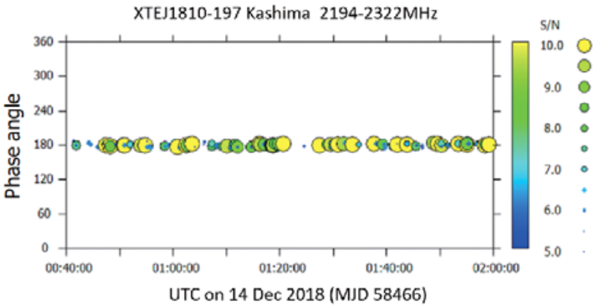

Figure 5. Pulses from the magnetar XTEJ1810-197 observed in Kashima are shown in the rotation-phase-UTC diagram. The rotation period on 14 December 2018 was 5.54143sec. Pulse intensities are shown in S/N with color-coded circles.

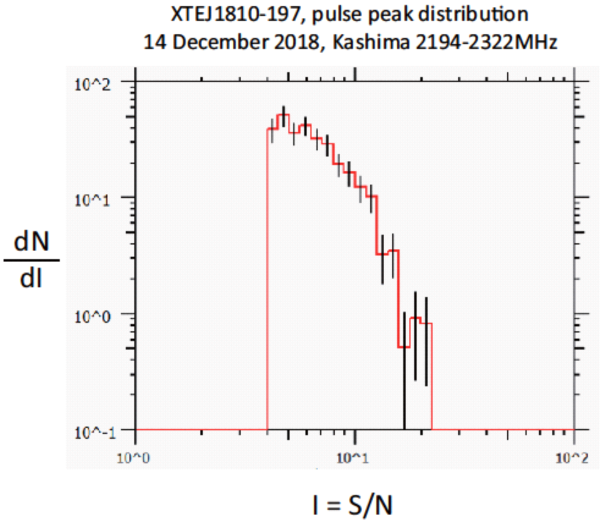

Figure 6. The flux distribution of the peak intensities of XTEJ1810-197 pulses in the 2.2-2.3GHz band.

6. Summary

As reviewed in preceding sections, the observational pulsar studies in Japan in the last 10 years were very successful. We hope to continue/expand this activity into the new era of the SKA/ngVLA projects.

7. Acknowledgments

We thank to all individuals who have contributed to this successful pulsar studies in the past 10 years (in alphabetical order);

T. Akahori, T. Aoki, K. Asano, Y. Asaoka, S. Eie, T. Enoto, K. Fujisawa, T. Hada, N. Hiroshima, T. Hirota, S. Hisano, M. Honma, H. Imai, W. Ishizaki, O. Kameya, K. Kashiyama, R. Kataoka, N. Kawai, S. Kisaka, H. Kita, E. Kobayashi, M. Kojima, T. Kondo, M. Kumamoto, S. Matsukiyo, R. Mikami, H. Misawa, R. Morita, Y. Murata, K. Nagata, K. Niinuma, H. Odaka, M. Oeda, Y. Ohira, T. Oyama, S. Oyama, Y. Sato, M. Sekido, S. Shibata, K. Takahashi, K. Takefuji, H. Takeuchi, Y.T.

Tanaka, S.J. Tanaka, K. Tawara, Y. Terada, M. Tokumaru, S. Torii, Y. Toyotome, F. Tsuchia, Y. Yamakoshi, R. Yamazaki, Y. Yonekura, N. Yonemaru, and T. Yoshida.

References

[1] Staelin, D. H., and E. C. Reifenstein III, Pulsating radio sources near the Crab nebula, Science, **162**, 1483, 1968.

[2] Hankins, T. H., and J. A. Eilek, Radio emission signatures in the Crab pulsar, ApJ, **670**, 693, 2007.

[3] Mikami, R., et al., Wide-band spectra of giant radio pulses from the Crab pulsar, ApJ, **832**, 212, 2016.

[4] Hitomi Collaboration (F.Aharonian et al.) and radio pulsar collaboration (T. Terasawa et al.), Hitomi X-ray studies of giant radio pulses from the Crab pulsar, PASJ, **70**, 15, 2016.

[5] Argyle, E., and J. F. R. Gower, ApJL, **175**, L89, 1972; Sallmen, S., et al., ApJ, **517**, 460, 1999; Cordes, J. M., et al., ApJ, **612**, 375, 2004; Bhat, N. D. R., S. J. Tingay, and H. S. Knight, Astrophys. J., Vol. ApJ, **676**, 1200, 2008; Karuppusamy, R., et al., AA, **515**, A36, 2010; Crossely, J. H., et al., ApJ, **722**, 1908, 2010; Majid, W. A. et al., ApJ, **741**, 53, 2011; Mickaliger, M. B., et al., ApJ, **760**, 64, 2012.

[6] Shearer , A., et al., Enhanced optical emission during Crab giant radio pulses, Science, **301**, 493, 2003.

[7] Strader, M. J. et al., Excess optical enhancement observed with ACRONS for early Crab giant pulses, ApJL **779**, L12, 2013.

[8] Lundgren, S. C., et al., ApJ, **453**, 433, 1995; Bilous, A. V., et al., ApJ, **728**, 110, 2011; Bilous, A. V., et al., ApJ, **749**, 24, 2012; Aliu, E., et al., ApJ, **760**, 136, 2012.

[9] Lyne, A. G., et al., 45 years of rotation of the Crab pulsar, MNRAS, **446**, 857, 2015.

[10] Shaw, B. et al., A large glitch in the Crab pulsar (PSR B0531+21), Atel #10939, 8 Nov. 2017.

[11] Jodrell Bank Crab Pulsar Monthly Ephemeris, `http://www.jb.man.ac.uk/pulsar/crab.html`.

[12] Shaw, B. et al., Mon. Not. Roy. Astron. Soc., Vol. MNRAS, **478**, 3832, 2018.

[13] Lyne, A. et al., Intense radio flare from the magnetar XTEJ1810-197, Atel #12284, 11 Dec. 2018.

Development of Wideband Antenna

Hideki Ujihara (*ujihara@nict.go.jp*)
Kashima Space Technology Center,
National Institute of Information
and Communications Technology,
893-1 Hirai, Kashima, Ibaraki 314-8501, Japan

1. Status of development

MARBLE1 and 2 with 2.4 m dish and NINJA feed were ready for intercontinental experiment of VLBI Time and Frequency Transfer, Gala-V. MARBLE1 was transported to Medicina radio observatory and set in the summer of 2018, and surface of 34 m was well adjusted by radio holography by broad cast satellite to start the experiment(Fig.1). In 2019, lens of the NINJA feeds was replaced to improve efficiency and reduce return loss. Figure 2 and 3 shows far-field beam patterns of the NINJA feed with new lens. They are more fitted to the subtended angle of the sub-reflector of the MARBLE, 52 degrees. Also a orthogonal mode transducer(OMT) was developed to reduce the return loss. Aperture efficiency of MARBELs are estimated to reach around 50 % by this upgrade and 34 m to around 40 %.

Figure 1.
Transported MARBLE1 from Kashima in Japan to Medicina radio observatory in Italy.

2. Plans

Development of novel water vapor radiometer has been started, which will realize rapid and accurate measurement of vapor, water and oxygen in the atmsphere 18-64 GHz by one reciever system with a wideband feed. Studies to extend the band width and improve of the efficiency of the wideband OMT and feed are still keeping to improve the performance of Gala-V and for other applocations.

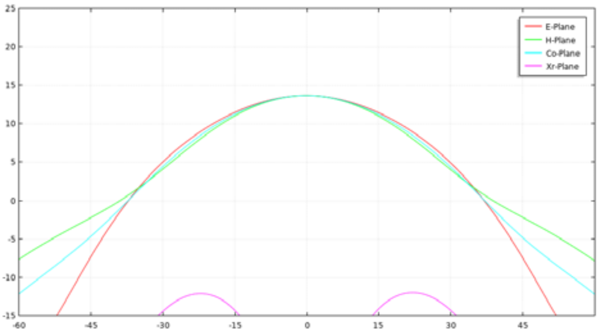

Figure 2.
Beam patterns of NINJA feed for MARBLE at 4.0 GHz(simulation).

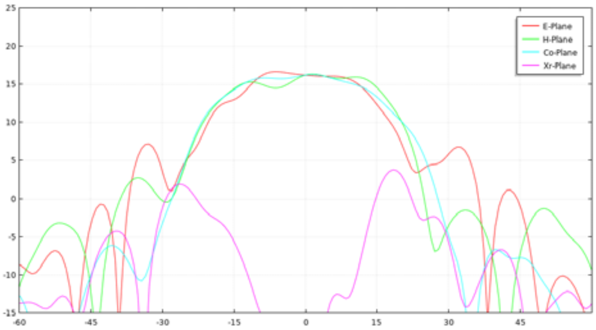

Figure 3.
Beam patterns of NINJA feed for MARBLE at 13.6.0 GHz(simulation).

References

[1] Ujihara, H., (2016) Development of wideband feed for Kashima 34m Antenna, Radio Sci., 52, doi:10.1002/2016RS006071

[2] Ujihara, H., Takefuji, K., Sekido M., and Ichikawa R.,(2018) "Development of Wideband Antennas", International Symposium on Advancing Geodesy in a Changing World, Proceedings of the IAG Scientific Assembly, Kobe, Japan, July 30 - August 4, 2017 (peer-reviewed), (10.1007/1345 2018 41).

Ten years of Ibaraki Station

Yoshinori Yonekura
(*yoshinori.yonekura.sci@vc.ibaraki.ac.jp*),

Center for Astronomy, Ibaraki University,
2-1-1 Bunkyo, Mito, Ibaraki, Japan

Abstract: Ten years have passed since the beginning of the conversion from two satellite communication antennas to radio telescopes in Ibaraki Station at 2009. I briefly summarize the history of the Ibaraki Station.

1. Introduction

The Takahagi and Hitachi 32 m antennas, which had been used for satellite communications at 4 and 6 GHz by KDDI, were decommissioned in 2007 March. These antennas were handed over to the National Astronomical Observatory of Japan (NAOJ) on 2009 January 31, and now belong to the Ibaraki station, which is a branch of the Mizusawa VLBI Observatory of NAOJ.

The Hitachi antenna was constructed in 1983 and the Takahagi antenna was constructed in 1992 by the Mitsubishi Electric corporation. The mechanics and surface of the antenna were not changed. The feed horn was newly designed and installed. By exchanging the bottom of the horn, we can change the observation band from the low-frequency band (6.7 and 8 GHz) to the high-frequency band (22 GHz) and vice versa. Antenna control software was newly developed. Two cryogenically-cooled receivers for 6–9 GHz and 20–25 GHz were equipped for each antenna. A hydrogen maser, wide-band recording systems, single-dish recording systems were also installed. For more details, please refer to Yonekura et al. (2016).

2. The Chronological Table of the Ibaraki Station

- 2009/Apr./23, First light of Hitachi antenna (drift-scan [no tracking] toward the Sun using 6.7 GHz room-temperature receiver and power meter) (fig. 1).
- 2009/Nov./24, Spectroscopic first light of Hitachi antenna (tracking a methanol maser source G9.62 using 6.7 GHz room-temperature receiver and spectrum analyzer) (fig. 2).
- 2010/Feb./25, First spectroscopic observation with Hitachi antenna (tracking a methanol maser source W3 using 6.7 GHz cryogenically-cooled receiver and sampler K5/VSSP32) (fig. 3).
- 2010/Jun./10, First fringe of Hitachi antenna with Mizusawa 20-m and Iriki 20-m antennas toward a methanol maser source G9.62 using 6.7 GHz cryogenically-cooled receiver with K4 back-end (DFC-2000, DIR-1000) (fig. 4).
- 2010/Jul./01, First light of Takahagi antenna (tracking the Sun using 6.7 GHz room-temperature receiver and power meter) (fig. 5).
- 2010/Aug., VLBI scientific operations with Hitachi antenna have started.
- 2011/Mar., Damaged by The 2011 off the Pacific coast of Tohoku Earthquake (fig. 6).
- 2012/Dec., Single-dish scientific operations with Hitachi antenna have started.

3. History of Back-end

History of back-end is summarized in fig 7.

4. Acknowledgments

We are grateful to NICT for the use of correlation software.

References

[1] Yonekura, Y., et al. 2016 PASJ, 68, 74.

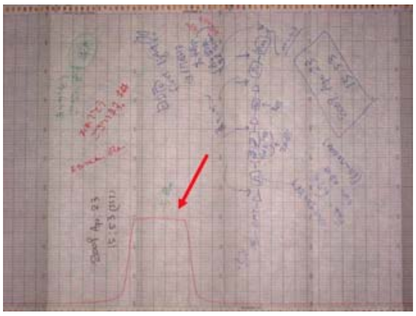

Figure 1. Hitachi first light.

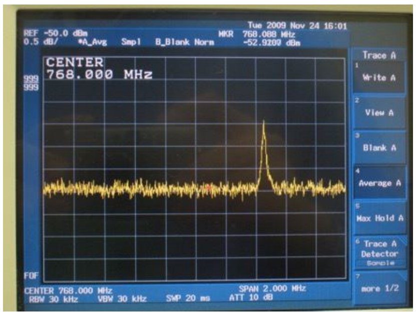

REF -50.0 dBm
0.5 dB/ *A_Avg Smpl B_Blank Norm
MKR 768.088 MHz
-52.9209 dBm
Tue 2009 Nov 24 16:01
CENTER 768.000 MHz
CENTER 768.000 MHz
RBW 30 kHz VBW 30 kHz SWP 20 ms
SPAN 2.000 MHz
ATT 10 dB

Figure 2. Hitachi spectroscopic first light.

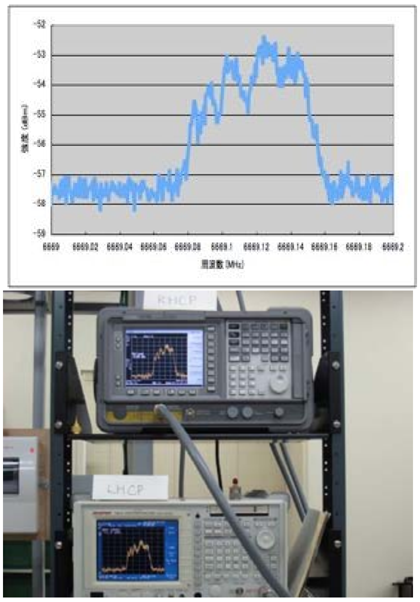

Figure 3. Hitachi first spectroscopic observation.

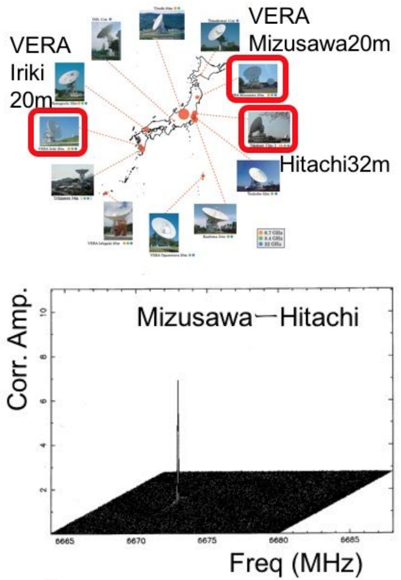

Figure 4. Hitachi first fringe.

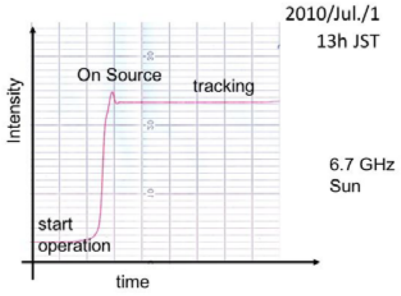

Figure 5. Takahagi first light.

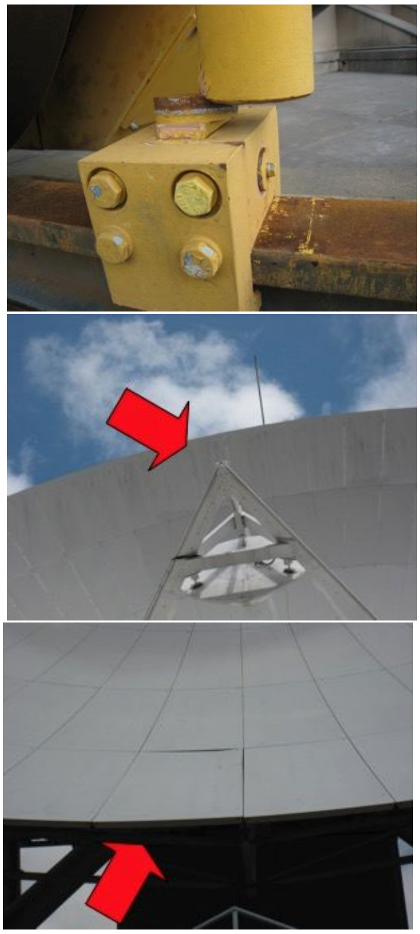

Figure 6. Damage by the earthquake.

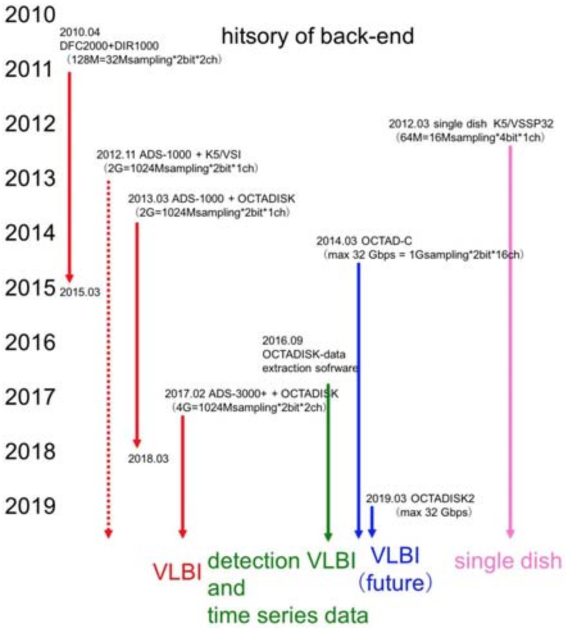

Figure 7. History of back-end.

- News - News - News - News -

Kashima 34-m Antenna

–Damaged by Typhoon No.15 (Faxai), 2019–

Mamoru Sekido (*sekido@nict.go.jp*) , *NICT*

Space-Time Standards Laboratory,
Kashima Space Technology Center,
893-1 Hirai, Kashima Ibaraki, Japan

1. Kashima 34-m Antenna and its Contributions

Kashima 34-m antenna was built in 1988 for ”Western Pacific VLBI Network” project[1], whose purpose is measurement of pacific plate motion and regional crustal movement around Japan.

This antenna was designed as dedicated VLBI station with multiple receiver systems. With the scope of not only geodetic VLBI but also for astronomical VLBI observations and R&D to explore the application of radio astronomical signal, many receiver systems were implemented at initial state: 1.35-1.75GHz, 2.1-2.35GHz, 4.6-5.1GHz, 8.18-8.6GHz, 7.86-8.36GHz, 10.2-10.7GHz, 14.4-14.9GHz, 14.9-15.4GHz, 21.88-22.38GHz, 23.58-24.08GHz, and 32.8-43.4GHz.

After accomplishment[3] of initial aim of the antenna installation, The Kashima 34-m antenna has contributed to many projects for radio astronomy and its applications. That include research on pulsar timing[4, 5] and astrometry[6], water maser survey[7], interplanetary scintillation observation to measure the solar wind speed[12, 13], Jupiter’s synchrotron radiation[10], and bistatic Rader observation of asteroids [8, 9]. To memorize the first success of this Rader observation, the target asteroid was named GOLEVKA, which came from the participated station’s names GOLdstone, EVpatoria, and KAshima. The antenna played important role to support the first space VLBI mission VSOP[11], and participated many other astronomical observations, but we cannot introduce all of them here because of limited space of this article.

Kashima 34-m antenna has participated geodetic VLBI sessions conducted by IVS(International VLBI Service for Geodesy & Astrometry), AOV(Asia-Oceania VLBI Group for Geodesy and Astrometry), and domestic geodesy sessions conducted by GSI(Geospatial Information Authority of Japan). In addition, Kashima 34-m has played important role in R&D researches for VLBI technology developments: such as development of PC-based VLBI data acquisition and correlation processing system K5[14], rapid UT1 determination by combination use of the K5 and highspeed internet[16, 17], and contribution to VSI-H and VDIF standards[15]. High sensitivity Kashima 34-m allowed to achieve these developments. In recent years, Kashima 34-m was upgraded as broadband antenna with newly developed broadband feed system. And it has been used for frequency comparison between optical time standards between INRiM(Italy) and NICT(Japan). The experiments were successful, and we expected to continue further sessions in winter of 2019.

Figure 1. Kashima 34-m station (top) and its receiver room(bottom).

2. Damage by Typhoon No.15 (Faxai)

Damages of typhoons becomes terrible year by year. We have prepared for strong wind by repair of main reflector backup-structure not to make any damages to surroundings, because it is located in residential area. However, the typhoon No.15 (Faxai) arrived on 9th Sep., 2019 was strongest ever experienced at our site. Maximum windspeed record was 56 m/s in station’s weather data. It was fortune that there was no damage to the surrounding houses.

In the evening before typhoon’s arrival, antenna was at zenith position as usual to prepare for strong wind. Although in the morning just after the ty-

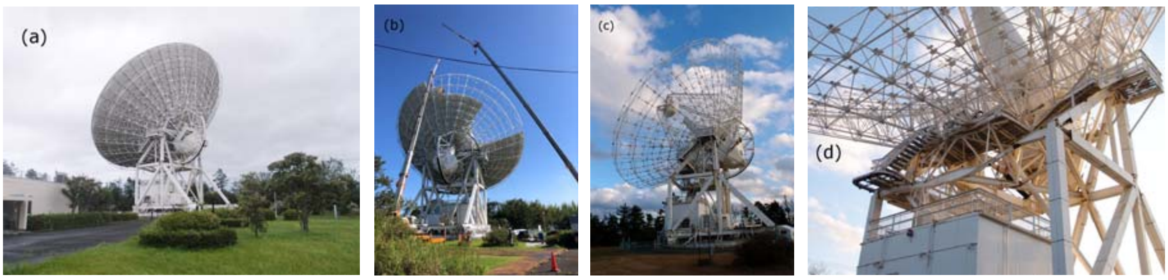

Figure 2. (a)Kashima 34-m antenna damaged in the morning of 9th Sep., 2019, (b)Main reflector panes were removed in the same month. (c) Picture as of December, 2019, (d) Damages at elevation driving motor, antenna structure, and working stage.

phoon has passed, we found that the main dish of the antenna inclined at elevation angle about 120 degrees, which moved over elevation angle limit of 90 deg. Then it was found that elevation driving motor, gearbox, and working stage were smashed. Because elevation motion was free and nothing supported elevation angle motion, we had to fix the elevation position by welding a thick steel plate immediately for safety. And finally, we removed the main reflector panels before arriving next coming typhoon.

This is the story of how the Kashima 34-m antenna was damaged, and why its shape was changed. Although the antenna operation stopped due to the damage of typhoon, closing of operation and dismantle of the antenna in 2020 has been decided before the disaster. Reason was increase of maintenance cost. It looks that Kashima 34-m antenna has gave glory to the last by herself before dismantling.

Acknowledgements

We wish thank to all the people supported the Kashima 34-m VLBI station. Especially, we thank to Y.Mizuno, Y.Watanabe, Y.Yamazaki, S.Suzuki, Y.Hirose of Rikei Co. Ltd, K.Ishizu, K.Nakazono, K.Nakazono, of Nakazono Co Ltd., H.Sakuyama, R.Suzuki of A.E.S Co Ltd., N.Kurihara, E.Kawai, J.Nakajima H.Takefuchi, H,Ohkubo of NICT, for direct involvement in maintenance, for keeping running, and for improving the Kashima 34-m antenna.

References

[1] Special Issue "Western Pacific Network", J. Commun. Res. Lab., Vol.42, No.1, pp.3-110, 1995.

[2] Imae M., et al., "The Main VLBI Station at Kashima", J. Commun. Res. Lab., Vol.42, No.1, pp.5-14, 1995.

[3] Koyama Y., J. Geod. Soc., Japan, **42**, 1, 43-57, 1996.

[4] Hanado, Y., et al., Publ. Astron. Soc. Japan, **54**, 305-313, 2002.

[5] Ilyasov, Yu. P., et al., Astrn. Lett., **31**, 30-36, 2005.

[6] Sekido, M. et al., Publ. Astron. Soc. Japan, **51**, 595-601, 1999.

[7] Takaba, H., et al., Publ. Astron. Soc. Japan, **53**, pp.517-533, 2001.

[8] Hudson R. S., et al., Icarus, **148**, 37-51, 2000.

[9] Koyama, Y., et al., "Rader Observations of Near Earth Asteroids 6489 Golevka and 4197 (1982 TA)", J. Comm. Res. Lab., Vol.48, No.1, 143-150., 2001.

[10] Miyoshi Y., et al., Geophys. Res. Lett., **26**, 9-12, 1999.

[11] Hirabayashi, H., et al., Publ. Astron. Soc. Japan, **52**, 997-1014, 2000

[12] Tokumaru M., et al., J. Geomag. Geolelectr., **43**, 619-630, 1991.

[13] Tokumaru M., et al., J. Geomag. Geolelectr., **46**, 835-849, 1994.

[14] Kondo, T., et al., J. Geod. Soc. Japan, **54**, 4, 233-248, 2008.

[15] Whitney, A., et al., Proc. IVS 2010 General Meeting, 192-196, 2010.

[16] Sekido, M., Earth Planets and Space, **60**, pp,865-870, 2008.

[17] Matsuzaka, S., et al., Proc. IVS 2010 General Meeting, 143-147, 2010.

"IVS NICT Technology Development Center News" (IVS NICT-TDC News) published by the National Institute of Information and Communications Technology (NICT) (former the Communications Research Laboratory (CRL)) is the continuation of "IVS CRL Technology Development Center News" (IVS CRL-TDC News). (On April 1, 2004, Communications Research Laboratory (CRL) and Telecommunications Advancement Organization of JAPAN (TAO) were reorganized as "National Institute of Information and Communications Technology (NICT)".)

VLBI Technology Development Center (TDC) at NICT is supposed

1) to develop new observation techniques and new systems for advanced Earth's rotation observations by VLBI and other space techniques,
2) to promote research in Earth rotation using VLBI,
3) to distribute new VLBI technology,
4) to contribute the standardization of VLBI interface, and
5) to deploy the real-time VLBI technique.

The NICT TDC newsletter (IVS NICT-TDC News) is published on a non-regular basis by NICT.

This news was edited by Mamoru SEKIDO, Kashima Space Technology Center. Inquires on this issue should be addressed to Mamoru SEKIDO, Kashima Space Technology Center, National Institute of Information and Communications Technology, 893-1 Hirai, Kashima, Ibaraki 314-8501, Japan, e-mail : sekido@nict.go.jp.

Summaries of VLBI and related activities at the National Institute of Information and Communications Technology are on the Web. The URL to view the home page of the Radio Astronomy Applications Section of the Space-Time Measurement Group of Space-Time Standards Laboratory is : **"http://www2.nict.go.jp/sts/stmg/ivstdc/news-index.html"**.

IVS NICT TECHNOLOGY DEVELOPMENT CENTER NEWS No.38, December 2019

International VLBI Service for Geodesy and Astrometry
NICT Technology Development Center News
published by
National Institute of Information and Communications Technology, 4-2-1 Nukui-kita, Koganei,
Tokyo 184-8795, Japan